AFRL-AFOSR-VA-TR-2023-0233

Investigation of the Effect of Crystallographic Anisotropy and Defects on the Electrocaloric Response of Stress-free Relaxor Ferroelectric Plates by Experimental and Analytical Techniques

MENSUR ALKOY, EBRU
GEBZE TEKNIK UNIVERSITESI TEKNOLOJI TRANSFER OFISI
CUHURIYET MAHALLESI, NO:2
GEBZE TEKNIK UNIVERSITESI TEKNOLOJI TRANSFER OFISI MUDURLUGU
KOCAELI, , 41400
TUR

12/21/2022
Final Technical Report

DISTRIBUTION A: Distribution approved for public release.

Air Force Research Laboratory
Air Force Office of Scientific Research
Arlington, Virginia 22203
Air Force Materiel Command

REPORT DOCUMENTATION PAGE

PLEASE DO NOT RETURN YOUR FORM TO THE ABOVE ORGANIZATION.

1. REPORT DATE	2. REPORT TYPE	3. DATES COVERED	
20221221	Final	START DATE 20180715	END DATE 20220714

4. TITLE AND SUBTITLE
Investigation of the Effect of Crystallographic Anisotropy and Defects on the Electrocaloric Response of Stress-free Relaxor Ferroelectric Plates by Experimental and Analytical Techniques

5a. CONTRACT NUMBER	5b. GRANT NUMBER	5c. PROGRAM ELEMENT NUMBER
	FA9550-18-1-0450	61102F
5d. PROJECT NUMBER	**5e. TASK NUMBER**	**5f. WORK UNIT NUMBER**

6. AUTHOR(S)
EBRU MENSUR ALKOY

7. PERFORMING ORGANIZATION NAME(S) AND ADDRESS(ES)
GEBZE TEKNIK UNIVERSITESI TEKNOLOJI TRANSFER OFISI
CUHURIYET MAHALLESI, NO:2
GEBZE TEKNIK UNIVERSITESI TEKNOLOJI TRANSFER OFISI MUDURLUGU
KOCAELI 41400
TUR

8. PERFORMING ORGANIZATION REPORT NUMBER

9. SPONSORING/MONITORING AGENCY NAME(S) AND ADDRESS(ES)
Air Force Office of Scientific Research
875 N. Randolph St. Room 3112
Arlington, VA 22203

10. SPONSOR/MONITOR'S ACRONYM(S)
AFRL/AFOSR RTB1

11. SPONSOR/MONITOR'S REPORT NUMBER(S)
AFRL-AFOSR-VA-TR-2023-0233

12. DISTRIBUTION/AVAILABILITY STATEMENT
A Distribution Unlimited: PB Public Release

13. SUPPLEMENTARY NOTES

14. ABSTRACT
Electrical measurements were made on random and textured samples reveal the impact of texture on the hysteresis and the dielectric response. When the P-E hysteresis loops of the random and textured ceramics in Fig.2. were compared, it was observed regardless of the measurement temperature that random ceramics had higher Pr and Pmax values and lower Ec values compared to the textured ceramics. This observation can be justified based on the development of a á001ñpc texture in a rhombohedral distorted perovskite. Application of an electric field to the 0.90PMN-0.10PT ceramics could be expected to induce a transition into a rhombohedral phase below the Tm. The spontaneous polarization direction in a perovskite with rhombohedral symmetry would be along the á111ñpc directions.

15. SUBJECT TERMS

16. SECURITY CLASSIFICATION OF:			17. LIMITATION OF ABSTRACT	18. NUMBER OF PAGES
a. REPORT	b. ABSTRACT	c. THIS PAGE		
U	U	U	UU	57

19a. NAME OF RESPONSIBLE PERSON	19b. PHONE NUMBER *(Include area code)*
ALI SAYIR	426-7236

Investigation of the Effect of Crystallographic Anisotropy and Defects on the Electrocaloric Response of Stress-free Relaxor Ferroelectric Plates by Experimental and Analytical Techniques

AFOSR Grant # FA9550-18-1-0450

PI: Dr. Ebru MENŞUR – ALKOY (Gebze Technical University)
Co-PI: Dr. Burç MISIRLIOĞLU (Sabancı University)

Final Report

Program Manager: Dr. Ali SAYİR

Participants

Principal Investigator: Prof.Ebru MENŞUR ALKOY
Orcid #: 0000-0001-7045-9771
Time in project: 3+1 years
Project role: All management of the project
Contribution to the project: All work done in the project
Collaboration: Related to this project, new study will be done with Prof.Daryossh Vashae

CO-Principal Investigator: Prof.I. Burç MISIRLIOGLU

Orcid #: 0000-0002-6054-0119

Time in project: 3+1 years
Project role: Management of the theoretical part of the project
Contribution to the project: Theoretical work in the project

Graduate Student: Ayşe BERKSOY YAVUZ

Time in project: October 201-March 2019
Project role: Graduate student (graduated and she became as assistant professor)
Contribution to the project: She had studied experimental part as fabrication of the PMN-PT and its texturing in various compositions.

Graduate Student: Gözde TOPRAK SÖZEN

Time in project: September 2018-March 2020
Project role: Graduate student (M.S-graduated)
Contribution to the project: She had studied experimental part as fabrication of the lead-free BCZT material and its texturing in various compositions.

Graduate Student: Ecem AYDIN

Time in project: September 2019-September 2020
Project role: Graduate student (M.S-graduated)
Contribution to the project: She had studied experimental part as fabrication of the 0.90PMN-0.10PT and its texturing in various compositions.

Graduate Student: İrem BÖBREK

Time in project: September 2019-September 2021
Project role: Graduate student (M.S-graduated)
Contribution to the project: She had studied experimental part as fabrication of the 0.72PMN-0.28PT and its texturing in various compositions.

Graduate Student: Tubanur AVCI

Time in project: September 2021-July 2022
Project role: Graduate student (current M.S. student)

Contribution to the project: She had studied experimental part as fabrication of the BZT and its characterization.

Graduate Student: Helin TEMEL

Time in project: September 2021-July 2022
Project role: Graduate student (current M.S. student)
Contribution to the project: She had studied experimental part as fabrication of the BCZT by sol-gel method and its characterization.

Graduate Student: Ahmet ÖZBEY

Time in project: September 2021-July 2022
Project role: Graduate student (current M.S. student)
Contribution to the project: He had studied experimental part as fabrication of the PVDF-BCZT polymer/ceramic composite and its characterization as a novel material for the potential electrocaloric application.

Graduate Student: Emre CANANOĞLU

Time in project: September 2021-July 2022
Project role: Graduate student (current M.S. student)
Contribution to the project: He had studied experimental part as fabrication of the epoxy-PZT polymer/ceramic composite and its characterization as a novel material for the potential electrocaloric application.

Other Partners and Collaborators
In this project, experimental part was done at the Laboratories of Department of Materials Science and Engineering in Gebze Institute of Technology and theoretical part was done by Sabanci University and Izmir Institute of Technology.

Dissemination:

Publications (SCI papers):

1. Namık Kemal Gözüaçık, Ebru Mensur-Alkoy, Sedat Alkoy, 'Efects of lanthanum doping on electrical and electromechanical properties of $(Pb_{1-x}La_x)(Zr_{0.70}Ti_{0.30})O_3$ ceramics', Journal of Materials Science: Materials in Electronics Volume 30, pp. 14045–14052, (2019), https://doi.org/10.1007/s10854-019-01769-0

2. Ömer Çakmak, Ebru Mensur-Alkoy, Gözde Toprak, Önder Tuna, Sedat Alkoy,' Investigation of the electrical properties of textured $0.5[Ba(Zr_{0.2}Ti_{0.8})]O_3–0.5[(Ba_{0.7}Ca_{0.3})TiO_3]$ piezoceramics', Journal of Materials Science: Materials in Electronics, Volume 31 pp. 4184–4192, (2020), https://doi.org/10.1007/s10854-020-02971-1.

3. Ebru Mensur-Alkoy, M. Baris Okatan, Ecem Aydin, Yusuf Kilic, I. Burc Misirlioglu and Sedat Alkoy 'Effect of texture on the electrical and electrocaloric properties of $0.90Pb(Mg_{1/3}Nb_{2/3})O_3–0.10PbTiO_3$ relaxor ceramics', Journal of Applied Physics, 128, 084102 (2020), https://doi.org/10.1063/5.0003296.
4. Irem Bobrek, Ayse Berksoy-Yavuz, M. Yunus Kaya, Sedat Alkoy, M. Barıs Okatan, I. Burc Misirlioglu, Ebru Mensur-Alkoy, 'Temperature Dependent Electrical and Electrocaloric Properties of Textured 0.72PMN - 0.28PT Ceramics', Integrated Ferroelectrics, Volume 223, 2022.
5. Namık Kemal Gözüaçık, Mustafa Çağrı Bayır, M. Baris Okatan, I. Burc Misirlioglu, SedatAlkoy, Ebru Menşur-Alkoy, 'Enhancement of the electrocaloric effect in $PbZr_{0.7}Ti_{0.3}O_3$ ceramics via La doping: Driven by phase co-existence or defect effects?', Acta Materialia, Volume 225, 11755915 February 2022, https://doi.org/10.1016/j.actamat.2021.117559.
6. M. B. Okatan, I. B. Misirlioglu, E. M. Alkoy and S. Alkoy, "Anisotropy of the electrocaloric effect in Pb,Mg,Nb,O3-PbTiO3 solid solutions" submitted to and rejected from Advanced Energy Materials in 2022, currently under revision for resubmission.

Oral Presentations:

1. Yusuf Kılıc, Sedat Alkoy, Ayse Berksoy-Yavuz, Ebru Mensur-Alkoy "Preperation and Characterization of Microstructurally Engineered Textured 0.90PMN-0.1PT Piezoelectric Ceramics", International Materials Technologies And Metallurgy Conference 2019(MTM2019), Istanbul-TURKEY (Oral).

2. Gözde Toprak, Ömer Cakmak, Sedat Alkoy, Ebru Mensur-Alkoy, "Electrical Properties of Random and Textured $0.8Ba(Zr_{0.15}Ti_{0.85})O_3$-$0.2(Ba_{0.8}Ca_{0.2})TiO_3$ Piezoelectric Ceramics Near the Triple Point", International Materials Technologies And Metallurgy Conference 2019(MTM2019), Istanbul-TURKEY (Oral).

3. Mustafa Yunus Kaya, Hüseyin Alptekin Sari, Ebru Menşur-Alkoy, Sedat Alkoy, "Structural and Electrical Properties of 0.65PNN-0.35PZT Ceramic Composition", International Materials Technologies and Metallurgy Conference 2019 (MTM2019), Istanbul-TURKEY (Oral).
4. Irem Bobrek, Ayse Berksoy-Yavuz, M. Yunus Kaya, Sedat Alkoy, M. Baris Okatan, I. Burc Misirlioglu, Ebru Mensur-Alkoy, 'Temperature dependent Electrical and Electrocalaric Properties of Textured PMN-PT Ceramics' The 5th International Conference on Smart Materials and Nanotechnology (SmartMat@2020) (Oral).
5. Ebru Menşur, 'What are the Challenges and What Dominates The Electrocaloric Performance in Lead-Based and LeadFree Ferroelectrics?', The 5th International Conference on Applied Physics and Materials Applications & Applied Magnetism and Ferroelectrics (ICAPMA-JMAG-2021). (Oral).
6. Irem Bobrek, Ayse Berksoy-Yavuz, M. Baris Okatan, I. Burc Misirlioglu, Ebru Menşur, 'Determination of Dielectric and Ferroelectric Response of Mn-Doped 0.72PMN -0.28PT Piezoceramics' Materials Thailand: AMF-AMEC 2021, (Temmuz 2021). (Oral).
7. Namık Kemal Gözüaçık, Ezgi Yalçın, Sedat Alkoy, Ebru Menşur-Alkoy, 'Nadir Toprak Elementi Katkılı Kurşun Nikel Niyobat-Kurşun Zirkonat Titanat Seramik Kompozisyonunun Elektrokalorik Özelliklerinin İncelenmesi', XI. Uluslarası Katılımlı Seramik Kongresi,21-23 Kasım 2022, Afyonkarahisar. (Oral).
8. Emre Cananoglu 'Synthesize of Lead-Based 67.5PMN-32.5PT Ceramic Powder with Structural/Electrical Characterization of PMN-PT-PU Composites', IWPMA, International Workshop on Piezoelectric Materials and Applications in Actuators 2022, 24-26th October 2022. (Oral).
9. Ebru Menşur, 'How Can the Electrocaloric Response in Ferroelectrics be Enhanced? Through Crystallographic Texture, or Point Defects, or Phase Coexistence?', E-MRS 2022 Fall Meeting, Warsaw (Poland) from September 19 to 22, 2022. (**Invited Talk**).

Poster Presentations:

1. Tubanur Avcı, Ebru Menşur, 'Electrical And Electrocaloric Properties Of Bzt With Critical Phase Points', 13 Ekim SERES 2021, V. Uluslararası Seramik, Cam, Emaye, Sır ve Boya Kongresi, SERES 21. https://www.seres2021.org/files/SERES-Bildiri-Kitabi-v2.pdf (Poster).

Proceedings in International Conferences:

1. Yusuf Kilic, Sedat Alkoy, Ayse Berksoy-Yavuz and Ebru Mensur-Alkoy, "Preperation and Characterization of Microstructurally Engineered Textured 0.9PMN-0.1PT Piezoelectric Ceramics", Proceedings of the International Materials Technologies and Metallurgy Conference 2019, Istanbul, Turkey, pp. 40-43 (2019).

2. Gözde Toprak, Ömer Cakmak, Sedat Alkoy, Ebru Mensur-Alkoy, "Electrical Properties of Random and Textured $0.8Ba(Zr_{0.15}Ti_{0.85})O_3$-$0.2(Ba_{0.8}Ca_{0.2})TiO_3$ Piezoelectric Ceramics Near the Triple Point", Proceedings of the International Materials Technologies and Metallurgy Conference 2019, Istanbul, Turkey, pp.71-74 (2019).

3. Mustafa Yunus Kaya, Hüseyin Alptekin Sari, Ebru Menşur-Alkoy, Sedat Alkoy, "Structural and Electrical Properties of 0.65PNN-0.35PZT Ceramic Composition", Proceedings of the International Materials Technologies and Metallurgy Conference 2019, Istanbul, Turkey, pp.79-82 (2019).

Book Chapter:

1. S. Alkoy, M. B. Okatan, I. B. Misirlioglu and E. Alkoy, "Electrocaloric Ceramics", to appear in Encyclopedia of Materials, published by Elsevier, 2022.

Thesis:

The following outcomes (AFOSR Supported completed M.S.thesis) are also reported:

1. Yusuf Kılıç, “Preparation and characterization of microstructurally engineered and textured 0.9PMN-0.1PT piezoelectric ceramics”, M.S. Thesis, Gebze Technical University (Graduated-2019).
2. Gözde Toprak Sözen, “Textured production and characterization of barium titanate based ferroelectric ceramic compositions with critical phase points in different Ca and Zr contents” Gebze Technical University (Graduated-2020).
3. Ecem Aydın, “Investigation of the electrocaloric properties of 0.90PMN-0.10PT textured thick films”, Gebze Technical University (Graduated-2021).
4. İrem Böbrek, “Investigation of electrocaloric properties of textured 0.72PMN-0.28PT thick fİlms”, Gebze Technical University (Graduated-2022).

Technical Report

Accomplishments

Research Objectives:

These objectives were mainly studied:

1. *Conduct a detailed study to establish structure-property relationship for the well-known systems:*

   -Indirect electrocaloric measurements have been conducted on the compositional systems that have been investigated so far especially for relaxor system of $0.90[Pb(Mg_{1/3}Nb_{2/3})O_3]–0.10[PbTiO_3]$ -PMN-PT. Effect of *texturing* on the elecrocaloric (ECE) properties was also investigated.

   $-0.72[Pb(Mg_{1/3}Nb_{2/3})O_3]–0.28[PbTiO_3]$ system was also studied to show the effect of the texturing on the ECE properties depending on crystal structure of the material.

2. *Clarify the effect of microstructure, composition, dopants etc. :*

   -Relaxor other lead based system of $(Pb,La)(Zr_{0.7}0Ti_{0.30})O_3$ -PLZT, has been studied. This PLZT system was modified for lower phase transition temperatures and effect of *defect chemistry* has been investigated in detail for the system.

3. Search for new, alternative ECE materials with relaxor FE compositions with higher ΔT. and search for materials that operate (i.e., with phase transitions) around room temperature.

   -Barium based BZT/BCZT systems were also investigated for ECE as promising lead-free system.

4. Investigation on the ECE with a view to understand the underlying mechanisms have been conducted. Analysis of the response of the electrocaloric response of the PMN-PT system was done.
5. Investigation on the electrical and ECE with a view to understand the underlying mechanisms have been conducted. Analysis of the effect of the point defect (La-doping). response of the PZT system was done.

Major Findings:

1. Effect of texturing on ECE properties:

0.90PMN-0.10 PT was fabricated as random and texture types by tape-casting method. The Curie temperature of this composition is around room temperature, which is advantageous for practical electrocaloric applications. The 0.90PMN-0.10PT composition is also a relaxor ferroelectric, a further advantage that is extending the temperature range of application. We synthesize randomly oriented and $\langle 001 \rangle_{pc}$ textured $0.90Pb(Mg_{1/3}Nb_{2/3})O_3$-$0.10PbTiO_3$ (0.90PMN-0.10PT) solid solutions that fall into the relaxor category. In Fig.1, XRD patterns of random and textured ceramics were given. A >%95% degree of $\langle 001 \rangle_{pc}$ texturing was achieved by use of single crystal $BaTiO_3$ template crystallites whose volume fraction do not exceed 5% of the entire sample volume.

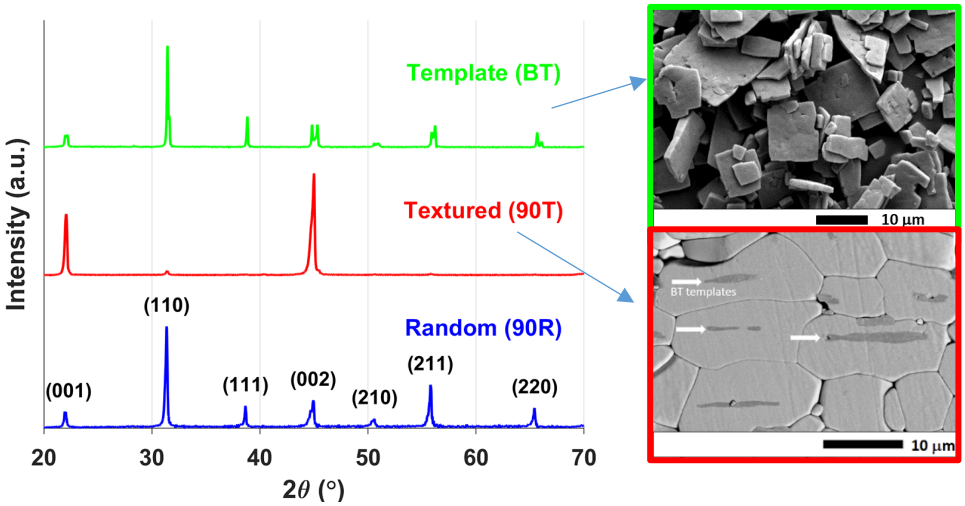

Figure.1: XRD patterns of textured and random ceramics of 0.90PMN-0.10PT ceramics. SEM micrographs of barium titanate (BT) templates and textured ceramic sample.

Electrical measurements were made on random and textured samples reveal the impact of texture on the hysteresis and the dielectric response. When the P-E hysteresis loops of the random and textured ceramics in Fig.2. were compared, it was observed regardless of the measurement temperature that random ceramics had higher P_r and P_{max} values and lower E_c values compared to the textured ceramics. This observation can be justified based on the development of a $\langle 001 \rangle_{pc}$ texture in a rhombohedral distorted perovskite. Application of an electric field to the 0.90PMN-0.10PT ceramics could be expected to induce a transition into a rhombohedral phase below the T_m. The spontaneous polarization direction in a perovskite with rhombohedral symmetry would be along the $\langle 111 \rangle_{pc}$ directions. However, when a perovskite piezoceramics with rhombohedral symmetry is textured along $\langle 001 \rangle_{pc}$ direction, which is the case in 0.90PMN-0.10PT, then, as

shown in the schematic drawing in Fig. 3, the $P_{r\langle 001\rangle}$ is expected to be $1/\sqrt{3}$ of the $P_{s\langle 111\rangle}$, with an angle of 54.7°. Whereas, in the case of random ceramics, the angles between P_r values of various grains and the $P_{s\langle 111\rangle}$ vary from 0° to 54.7°. Thus, randomly oriented ceramics are expected to have a higher P_r value on average compared to $\langle 001\rangle_{pc}$ textured materials when the base symmetry is rhombohedral symmetry. This was clearly observed in the current study, where P_r and P_{max} values of $\langle 001\rangle_{pc}$ textured 0.90PMN-0.10PT ceramics were lower than that of the random 0.90PMN-0.10PT ceramics, as shown in Fig. 2(b) & 2(c), where polarization values obtained from P-E hysteresis measurements taken at various temperatures ranging from 90°C to 0°C are given in Fig. 4(a) and (b), respectively, for random and textured 0.90PMN-0.10PT ceramics. The decrease could also be associated with hindered domain motion due to local constraints induced by the template $BaTiO_3$ crystals inside the grains. The increase that was observed in the case of E_c with texture, on the other hand, indicated that domain wall motion and polarization switching became more difficult. This might again be attributed to the clamping effect that arises from BT templates due to the existence of increasing interfacial stresses.

When the results presented in Fig. 5. are evaluated within this context, the preferred orientation to obtain higher electrocaloric performance from textured ceramics with rhombohedral symmetry should be the $\langle 111\rangle_{pc}$ direction, not the $\langle 001\rangle_{pc}$ direction. Although, texturing along the $\langle 001\rangle_{pc}$ direction does increase the piezoelectric properties drastically, compared to the random ceramics, as we also have previously observed in the PMN-32.5PT system. However, since the BT templates with tetragonal perovskite structure can usually be synthesized with major faces parallel to the (001) crystallographic planes, it does not seem possible to texture this material along $\langle 111\rangle_{pc}$. Though, it might be possible to cut a $\langle 001\rangle_{pc}$ textured ceramic along specific directions, so that the poling direction is along [111]. As a final note, both the random and textured ceramics have a common feature where the ΔT makes a plateau between 40-80°C which would make them rather useful for device applications in a wide temperature range, as expected of electrocaloric materials with a relaxor ferroelectric character.

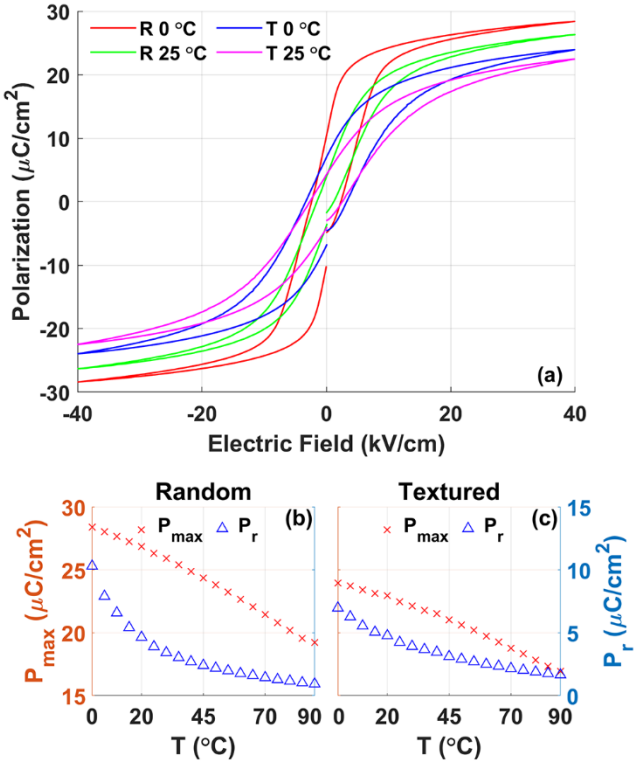

Figure. 2. (a) Electric field induced polarization graphs of random and textured samples at RT and 0°C. Variation of the remanent (E=0) and maximum polarization (E=40 kV/cm) with respect to temperature for (b) random and (c) textured ceramics.

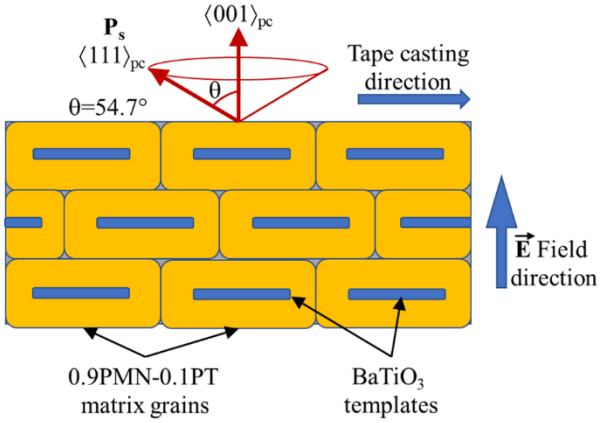

Figure. 3. Schematic drawing showing the orientational relationships in textured 0.90PMN-0.10PT.

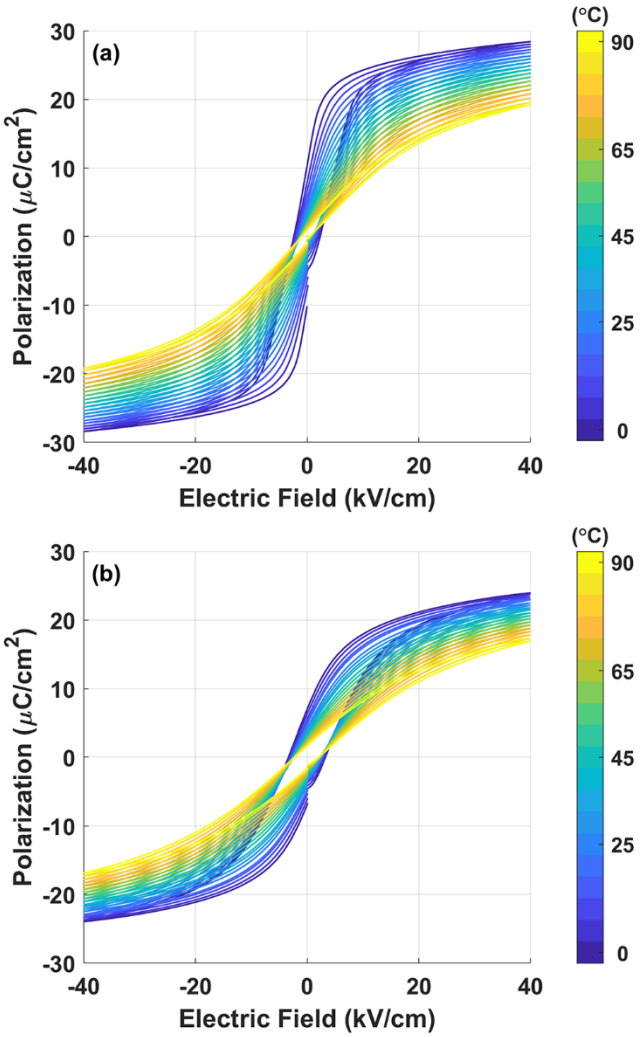

Figure. 4. Electric field induced polarization graphs of (a) random and (b) textured 0.90PMN-0.10PT samples measured at different temperatures.

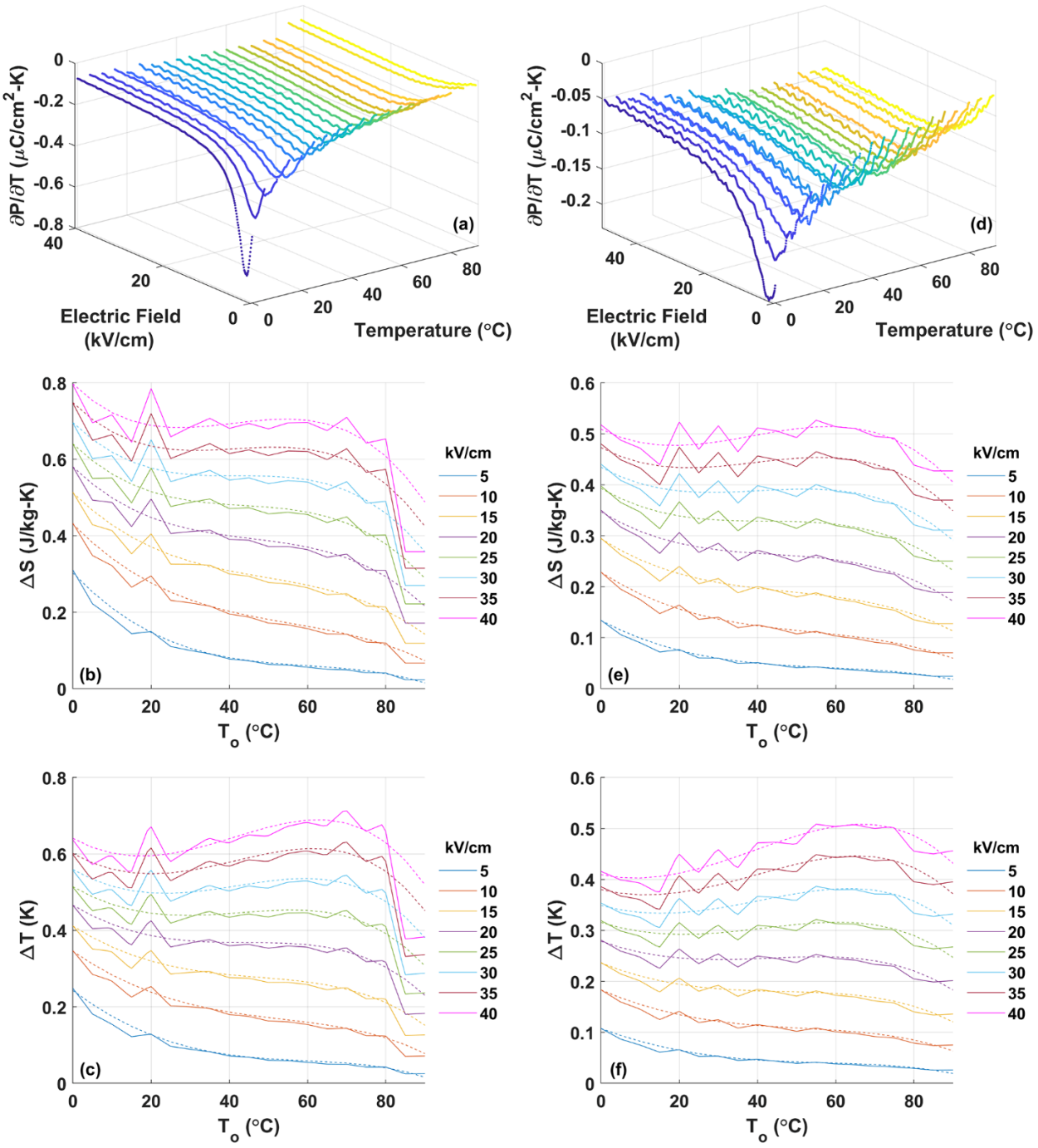

Figure. 5. (a, d) Pyroelectric coefficient, **(b, e)** ΔS vs T_o and **(c, f)** ΔT vs T_o plots of **(a-c)** random and **(d-f)** $<001>_{pc}$ textured 0.90PMN-0.10PT ceramics. In **(c,d)** and **(e,f)** solid and dashed lines represent, at several electric field strengths, E_2, (E_1 = 0 kV/cm), respectively, results based on use of pyroelectric coefficient determined via interpolation and 4th order polynomial fits.

As a conclusion of this part, the Curie-Weiss analysis show that the γ coefficients extracted from curve fits are consistent with a relaxor type behavior. We estimated the ECE from the experimental

data available and observed that textured samples have a lower ΔT compared to the randomly oriented samples possibly due to the non-preferable texture direction which causes a decrease in the ferroelectric properties, as well as the constraints induced by the template particles. To understand the extent to which the secondary effects might govern the ECE, we carried out a thermodynamic analysis using the Landau theory of phase transitions with the phenomenological coefficients acquired from published data in literature for the composition of interest. There is about 2-3 times difference between the theoretically calculated single crystal ECE and that of experimentally measured for the system studied here including previous reports. Experimental data shows that texturing these structures along $\langle 001 \rangle_{pc}$, while good for some of the properties such as the piezoelectric coefficient, might not be an effective option to enhance the ECE.

Main question: Due to the mismatch in the symmetry of the **E** and $\mathbf{P_s}$, lower $\mathbf{P_r}$ and lower $\mathbf{\Delta T}$ was observed in 0.90 PMN-0.10 PT textured ceramics. Why?

Solution approach: Because 0.90 PMN-0.10 PT system crystallized in rhombohedral symmetry. Spontaneous polarization and crystallographic texture directions can see in Fig.6 as given below.

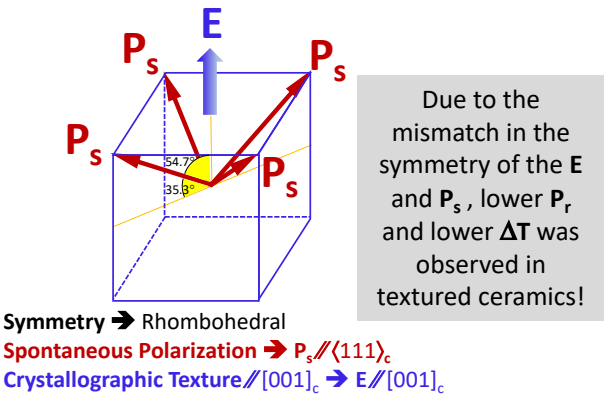

Figure 6: P_s directions for a rhombohedral unit cell.

For higher properties with texturing for ECE behavior, the ceramic sample crystallized as followings:

- $\langle 111 \rangle_c$ Textured Rhomboderal Phase
- $\langle 001 \rangle_c$ Textured Tetragonal Phase
- Changing the symmetry of E field

Experimental design for the approach: A system was chosen that provides the properties given above.

2. Effect of crystallographic orientation and direction of electric field on ECE properties:

0.72PMN-0.28PT system was chosen to investigate and compare its properties to 0.90 PMN-0.28 PT composition. As seen in the phase diagram given below (Fig.7) , 0.72PMN-0.28PT was chosen as near morphotropic phase boundary (MPB).

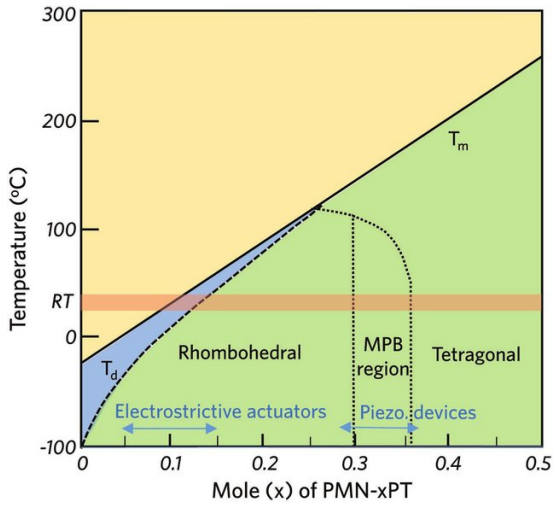

Figure.7. Phase diagram of PMN-PT.

The XRD analyses of random (R) and textured (T) ceramics were given in Fig. 8. These two ceramics were crystallized in perovskite phase without any secondary phases. It was seen from Fig.8 that the random ceramic had the highest intensity for $(110)_{pc}$ peak, as expected from the perovskite structure, while the intensities of the $(110)_{pc}$ and other (*hkl*) peaks of textured ceramics decreased with the development of texture. The intensities of (00*l*) peaks increased sharply in the textured ceramics. The Lotgering factor, *f*, of textured ceramics was approximately calculated as 80% for this system. In order to evaluate the symmetry of the random and textured ceramics, the (111) and (002) peaks of both random and textured ceramics have been investigated in detail by slow XRD scans with finer steps. Peak splitting is expected in the (111) peak in the case of rhombohedral symmetry, which is expected to be the case for the compositions with $PbTiO_3$ content lower than the morphotropic phase boundary composition. Splitting in the (002) peak is

expected in the case of tetragonal structure, which might be observed if the BT template particles stabilize a tetragonal symmetry. Detailed scans did not reveal any splitting in either case. This is believed to be due to the proximity of the composition of interest to the morphotropic phase boundary composition, where the structural symmetry is expected to be pseudo-cubic.

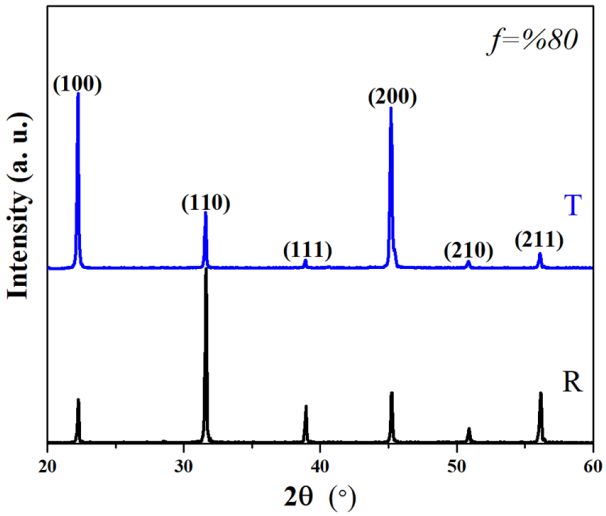

Figure 8. XRD patterns of random and textured ceramics with 0.72PMN-0.28PT composition.

Pyroelectric coefficients, ΔS vs T_o and ΔT vs T_o plots for the random and $\langle 001 \rangle_{pc}$ textured PMN–28PT ceramics were given in Figs. 7(a)–7(c) and 7(d)–7(f), respectively. From these figures the maximum ΔT_{EC} determined indirectly from the temperature dependent P-E measurements within the range of measurement temperatures were found to be around 0.5 K under 60 kV/cm electric field. The ΔT_{EC} values obtained from the textured ceramics was slightly (~10%) higher compared to the random case. The ΔT_{EC} values are expected to be higher close to the phase transition temperature, which is around 130°C in the current case and it was beyond the upper limit of our measurement setup. Additionally, in the perovskite relaxor ferroelectric materials, the ΔT_{EC} was reported to reach its highest values of 2-3 K under electric field amplitudes ranging from 60 to 90 kV/cm, which were the amplitudes for an electric-field-induced ferroelectric phase transition. Due

to the lower breakdown fields of the samples in our samples, field levels beyond 60 kV/cm have not been tried.

Although, a limited enhancement was observed with the development of texture, the crystallographic orientation of the grains and the applied field direction, both of which were along the $\langle 001 \rangle_{pc}$ direction, was unfavourable due to the inherent spontaneous polarization direction of composition of interest. Although, PMN-28PT is at the vicinity of the MPB, it is still on the rhombohedral side of the boundary and in a composition with rhombohedral symmetry, the spontaneous polarization would be along the $\langle 111 \rangle_{pc}$ directions. Thus, $P_{r\langle 001 \rangle}$ is expected to be misoriented from the P_s with an angle of 54.7° and scales up to $1/\sqrt{3}$ of the P_s in textured ceramics, whereas the angles between the P_r values of various grains and the P_s vary from 0° to 54.7° in the case of random ceramics. Thus, the observed polarization values in a $\langle 001 \rangle_{pc}$ textured ceramic would be expected to be lower compared to a $\langle 111 \rangle_{pc}$ textured case when the base symmetry is rhombohedral. This might also reflect positively on the ECE response of the textured ceramic. Investigation of the anisotropy of ECE in single crystals in the PMN-PT system with rhombohedral symmetry, such as 0.75PMN–0.25PT [5] and 0.76PMN–0.24PT [19] indicated that crystals cut along the $\langle 111 \rangle_{pc}$ directions displayed a relatively higher electrocaloric performance over the crystals cut along $\langle 110 \rangle_{pc}$ and $\langle 100 \rangle_{pc}$ directions. In the case of textured PMN-28PT ceramics in our study, there is a clear crystallographic orientation of grains along the $\langle 001 \rangle_{pc}$ direction, however, the $\langle 111 \rangle_{pc}$ directions of these grains are oriented along a cone of equal possibility, as shown in Figure 10(a) & 10(b). Nevertheless, an electric field applied along a direction perpendicular to the crystallographic texture direction, i.e. $E \perp \langle 001 \rangle_{pc}$ should be expected to induce a more favourable orientation of the P_r with P_s since a direction parallel to $\langle 001 \rangle_{pc}$ would have an angle of 35.3° with the P_s, which is along the $\langle 111 \rangle_{pc}$ direction. To investigate the validity

of this axiom thicker (t ≈ 3mm) samples were prepared from the textured ceramics. Although, the field handling of the thicker textured samples was lower than the thinner ones due to possible densification issues, the results were informative in themselves. As a reference of standard, samples were cut from the thick ceramic piece and electrode in the usual way, as shown in Figure 8(a), which was identified as $E \parallel \langle 001 \rangle_{pc}$. In the second set of samples, called the $E \perp \langle 001 \rangle_{pc}$, electrodes were coated parallel to the texture direction and thus, electric field was applied perpendicular to the crystallographic texture direction, as shown in Figure 10(b). A clear difference, i.e. anisotropy was observed in the P-E hysteresis loops where the P_r and P_{max} values of the $E \perp \langle 001 \rangle_{pc}$ samples were higher compared to the $E \parallel \langle 001 \rangle_{pc}$, as shown in Figure 10(c) and 10(d) for measurements taken at 20°C and 90°C, respectively. This difference was found to reflect positively on the EC response of the $E \perp \langle 001 \rangle_{pc}$ case where slightly higher ΔT_{EC} values were observed. *These results indicated that texturing PMN-PT ceramics with rhombohedral symmetry along $\langle 111 \rangle_{pc}$ direction should further enhance the electrocaloric response as we proposed.*

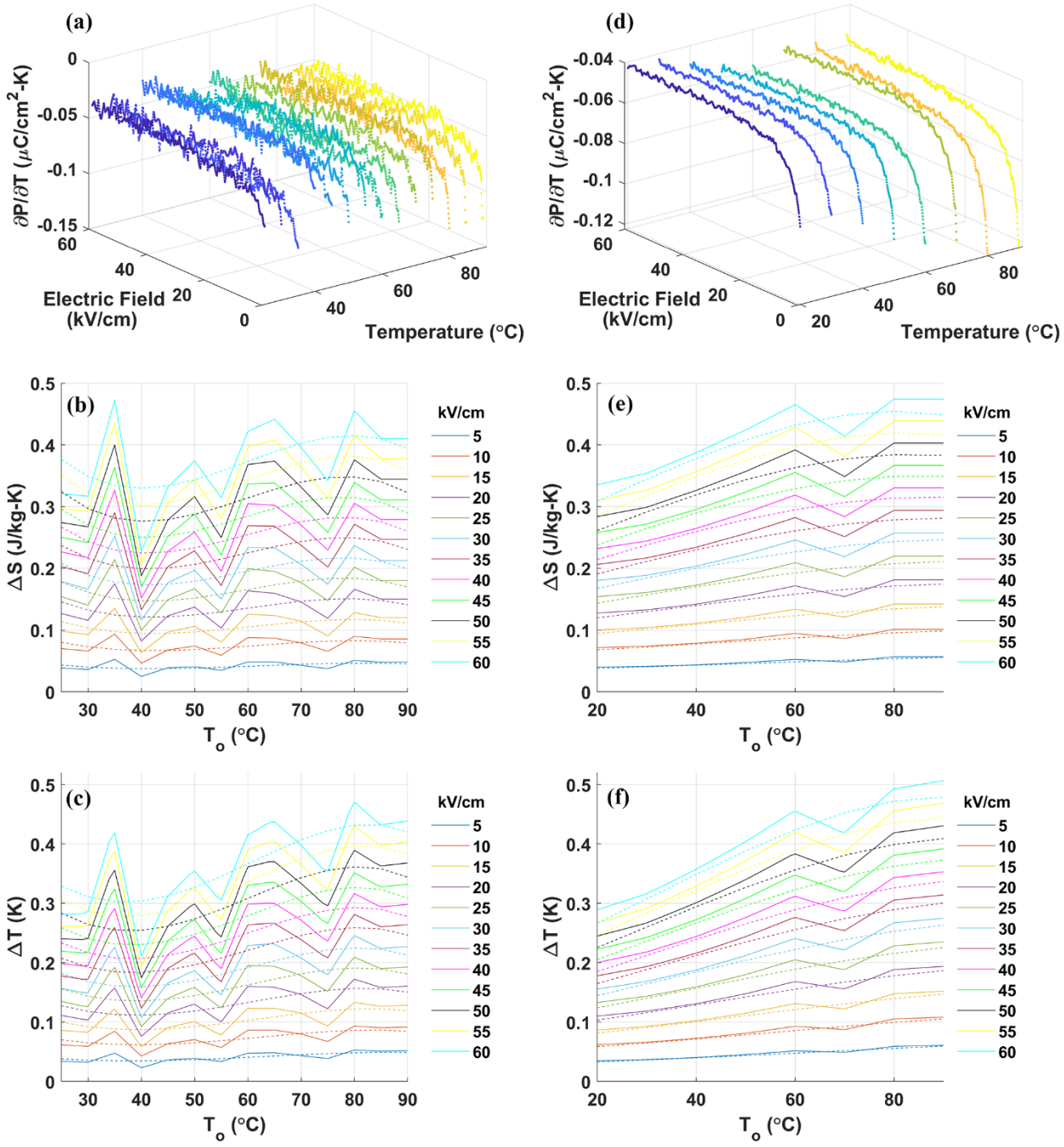

Figure 9. (a) and (d) Pyroelectric coefficient, (b) and (e) ΔS vs T_o and (c) and (f) ΔT vs T_o plots of (a)–(c) random and (d)–(f) ⟨001⟩pc textured PMN–28PT ceramics. In (c), (d) and (e), (f) solid and dashed lines represent, at several electric field strengths, E_2 and (E_1 = 0 kV/cm), respectively, results based on use of pyroelectric coefficient determined via interpolation and fourth order polynomial fits.

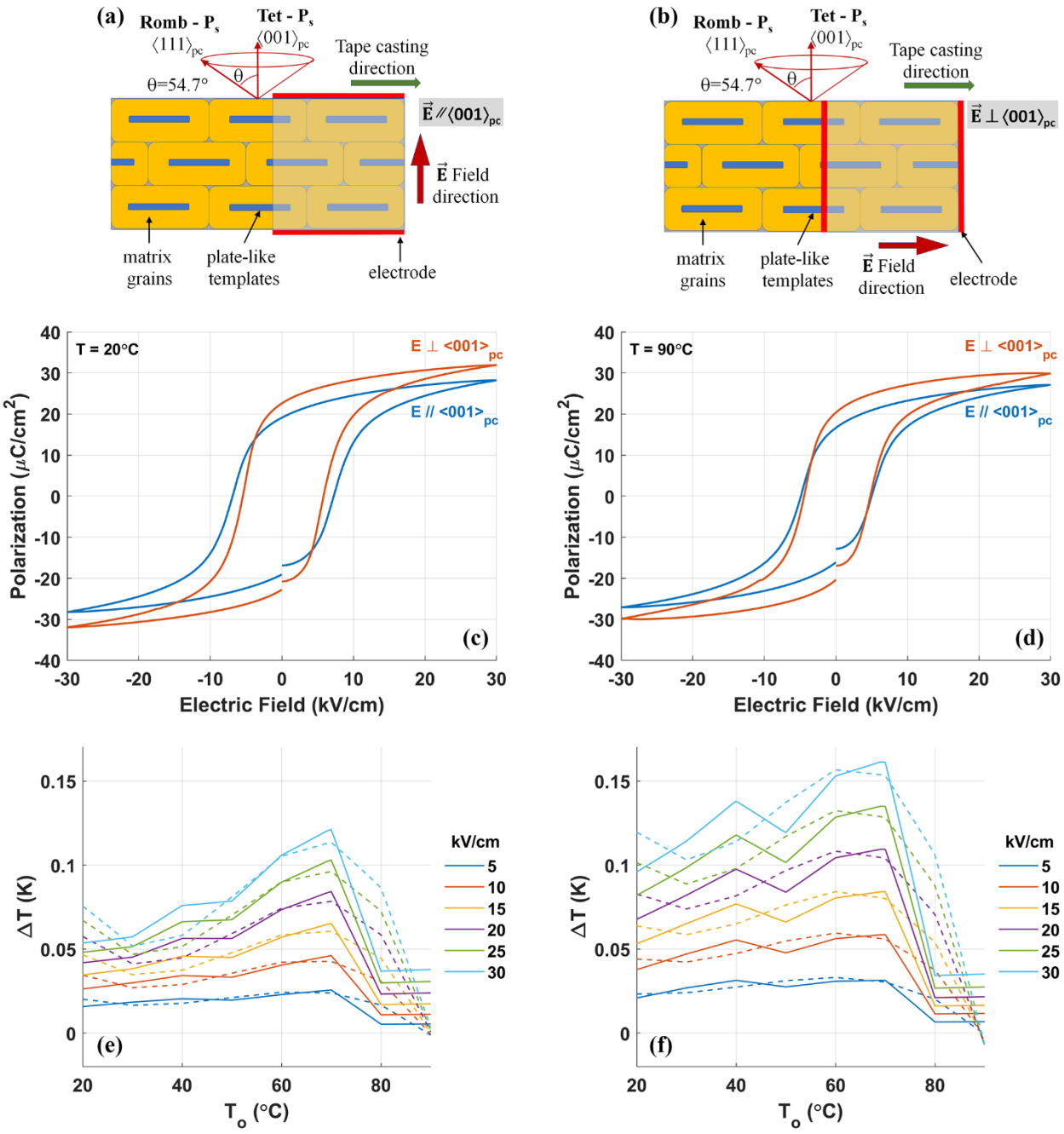

Figure 10. Textured PMN-28PT samples cut parallel and perpendicular to ⟨001⟩$_{pc}$ directions.

As a result, although, crystallographic texture along ⟨001⟩$_{pc}$ direction did improve the electrocaloric response of the PMN-28PT ceramics, the texture direction was not found to be entirely favorable, and that a texture along ⟨111⟩$_{pc}$ would be expected to yield a better

electrocaloric response due to the $\langle 111 \rangle_{pc}$ orientation of the spontaneous polarization direction in the composition with rhombohedral symmetry.

3. Effect of effect of microstructure, composition, dopants on the ECE properties:

Main question: Due to the mismatch in the symmetry of the **E** and $\mathbf{P_s}$, lower $\mathbf{P_r}$ and lower $\mathbf{\Delta T}$ was observed in 0.90 PMN-0.10 PT textured ceramics. Why?

Solution approach: Because 0.90 PMN-0.10 PT system crystallized in rhombohedral symmetry. Spontaneous polarization and crystallographic texture directions can see in Fig.6 as given below. Lattice defects and their effects have been pivotal in studies of phase transitions in a wide range of materials. Introduction of such defects into a ferroelectric material through doping of secondary elements can be tailored towards specific applications but the mechanism through which the bulk properties change is seldom scrutinized. Here, the effect of systematic La substitution into $PbZr_{0.7}Ti_{0.3}O_3$ (PZT 70/30) ceramics were studied and the temperature dependent properties and estimated the temperature changes under induced an external electric field was examined on the electrocaloric effect (ECE). Expecting the entropic changes to be maximal under an applied field, the suitability of the La doped PZT 70/30 system for EC applications had been a motivation to undertake the current task as this composition reportedly can host a rich variety of phases depending on La content including relaxor and antiferroelectric (AFE) states.

The compositional range that was investigated in this study, partially AFE-like hysteresis loops at RT under applied electric field were observed firstly for the composition with 8 mol% La, as shown in Fig. 11. Beside this, a strong decrease of remnant polarization (Pr) was observed in the hysteresis with a relatively gradual increase in the La content, and this behavior can be associated with the relaxor character becoming especially dominant after this La content (Fig. 11). Another possibility could be the location of the PZT composition being in the vicinity of the FE/AFE phase boundary. Doping the PZT 70/30 in this work beyond 8-mol %, polarization loops at RT continued to become slimmer with no sign of an AFE behavior. In addition to local strain fields generated, the randomly distributed La-sites also are considered to act as donors with neighboring acceptors to sustain

charge neutrality, forming dipole-defect complexes. Dependence of the hysteresis of the 2D lattice on the La-site concentration are displayed in Figure 12.

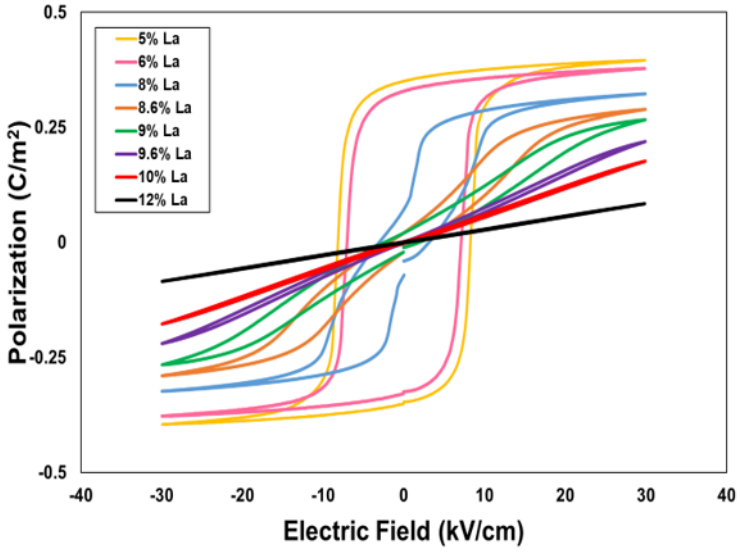

Figure 11. RT hysteresis of PLZT ceramics with various La concentration.

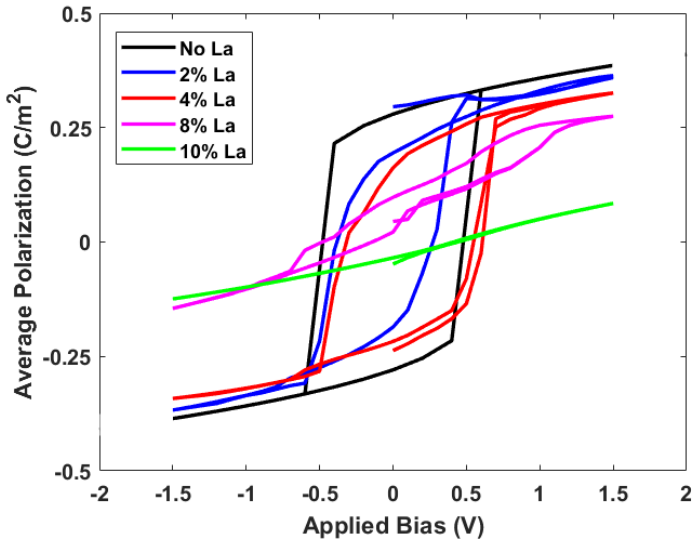

Figure 12. Simulated RT hystereses for various La concentrations in the 2D grid using the method prescribed in Sect. II b. The average polarization implies the component along the field direction (P_3 in this case).

An electrocaloric (EC) temperature change of 1.15°C in a wide range of temperatures for 8% La doping at 45 kV/cm applied field was estimated from experimental data, the possible origins of

which is discussed (Fig. 13). We were able to explain the experimental results by adopting a Landau-Ginzburg based computational approach coupled with elasticity and electrostatics whereby La sites are treated as point defects in a PZT 70/30 lattice. The gradual slanting of the hysteresis and reduction of the transition temperature in the samples with increasing La content is claimed to be a direct consequence of the electrical fields due to formation of dipolar defect complexes as backed by our simulations. The ECE is discussed in the light of the simulations and recent results for AFE ceramics. With increasing La content, properties start to deviate from that of pure PZT 70/30 substantially that are describable by the La sites in the lattice acting as defect-dipole complexes as revealed by thermodynamic simulations. Some of the findings we report are in contrast with the phase diagram proposed for the La-rich (>9-10%) PZT 70/30 that is also supported, albeit indirectly, by our EC analyses. Even when reaching the fields near the break down limit of PZT 70/30, we have neither observed an AFE-to-FE transition in the hysteresis nor a sudden change in the EC response that one would expect because of a field induced AFE-to-FE transition. The reduction and smearing of the transition temperature agree with what one would expect from an increasing concentration of lattice defects in a ferroelectric, a conjecture which we tried to prove via thermodynamic simulations. We also note that there appears to be an optimal concentration of La doping to obtain ΔT values exceeding 1K or more that is sustainable in a wide temperature range that is desirable for ECE devices. This optimal concentration falls in the phase regime where the stable state is ferroelectric with a smeared transition temperature around 85°C. Further smearing of the transition beyond 8%La concentration results in a weaker ΔT in the entire applied electric field range, likely driven by the stabilization of the paraelectric or a weak polar phase.

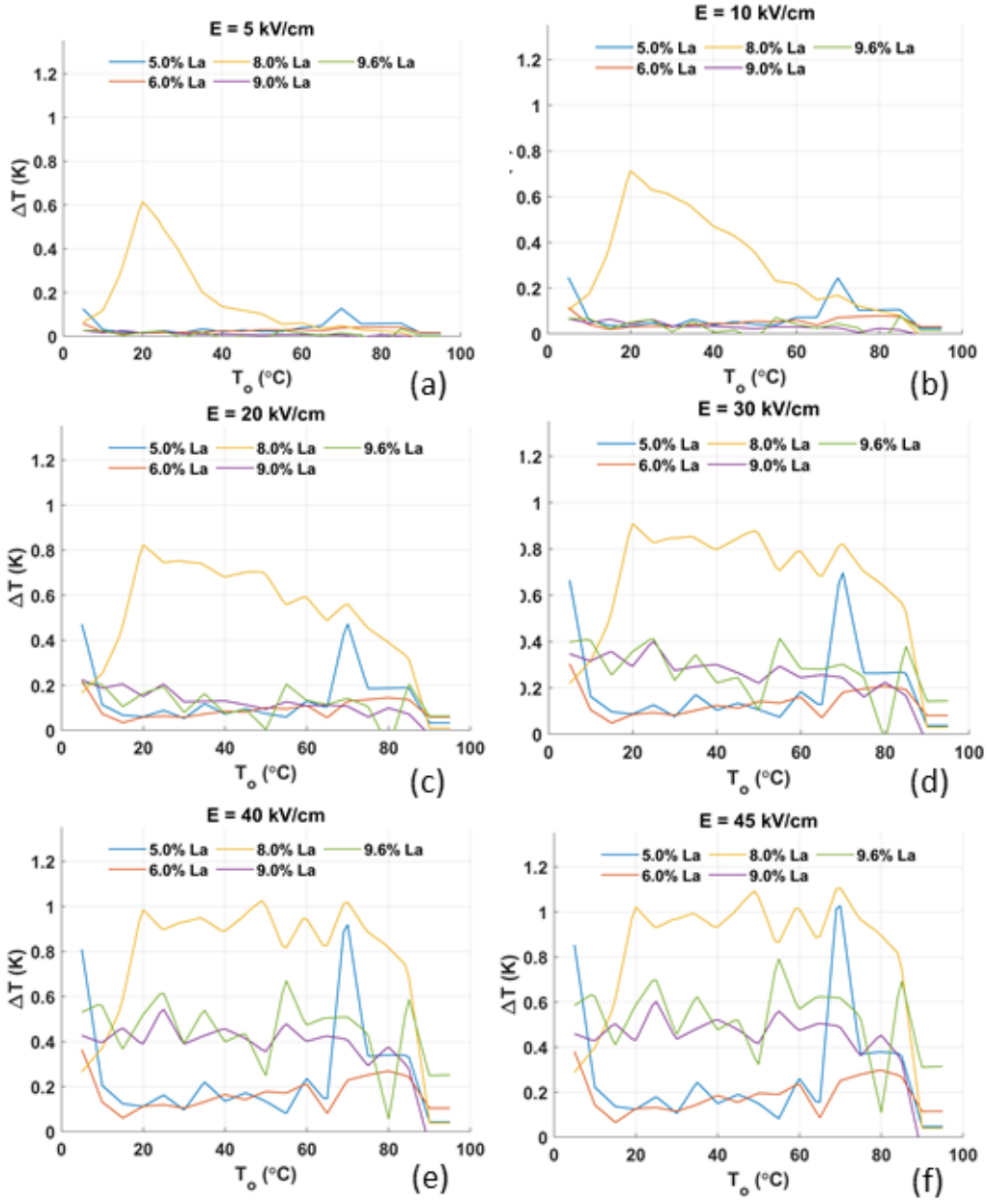

Figure 13. Temperature changes, ΔT, extracted from temperature dependent experimental data using the formulation in Eq. 1 for different applied strengths. T_o denotes the starting temperature at which the field was gradually increased until reaching a specified limit. Each limit of the applied field is given on each plot.

4. Analysis of the electrocaloric response of the PMN-PT system

Main question: How does the ECE properties change by composition of the PMN-PT?

One of the first tasks, in parallel with the indirect measurement analysis of the synthesized PMN-PT samples, the group undertook was the analysis of the anisotropy effects in a broad sense. This was mainly due to our aim in providing an informative picture on a range of compositions and to see if the compositions near the morphotropic boundary had a more pronounced EC response at least from the theoretical perspective. Below we provide a summary of some representative results after conducting a systematic computational study on the effect of texture, i. e., anisotropy on the EC response of bulk (1-x)Pb(Mg1/3Nb2/3)O3-xPbTiO3 (PMN-PT) compositions using a Landau-like theory applied to ferroelectrics. As this system contains a morphotropic phase boundary (MPB) in the vicinity of which the anisotropy of ferroelectric polarization on the rhombohedral side vanishes, we specifically focus on compositions touching this boundary. The temperature-composition phase diagram of PMN-PT given in Figure 14 for convenience.

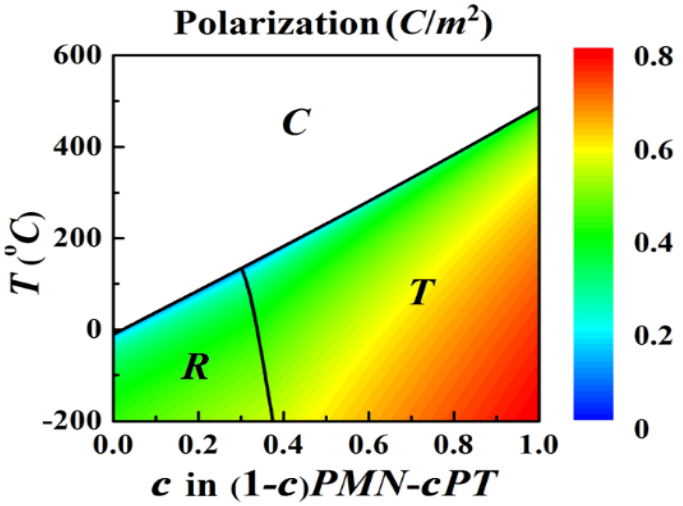

Figure 14. Computed composition-temperature phase diagram of PMN-PT. The boundary between R and T phases were considered to be the region of highest ECE as the anisotropy energy around these compositions tend to vanish, allowing large entropic changes upon field application a possibility (Diagram from Heitmann & Rossetti, J. Am. Ceram. Soc. 97, 1661–1685 (2014)).

In this project, we employ a Landau-like theory of phase transitions considering the 6th order polynomial of polarization to account for the presence of a first order transition. Using the potential reported in Heitmann & Rossetti, J. Am. Ceram. Soc. 97, 1661–1685 (2014) and Khakpash, N.,

Khassaf, H., Rossetti, G. A., and Alpay, S. P., Appl. Phys. Lett. 106, 082905 (2015), we went on to estimate the EC response of the PMN-PT as a function of temperature and direction of applied electric field with various max. amplitudes. The electrocaloric response, ΔT (change in temperature T) of a system under thermodynamic equilibrium can be expressed as:

$$\Delta T = -\int_{E_1}^{E_2} \frac{T}{C\rho}\left(\frac{\partial P}{\partial T}\right)_E dE \quad (1)$$

between initial, E_1, and final, E_2, values of the electric field strength, E, where C, ρ and $\left(\frac{\partial P}{\partial T}\right)_E$ are, respectively, the heat capacity, density and the pyroelectric coefficient of the material. The above equation relies on the Maxwell relation $\left(\frac{\partial S}{\partial E}\right)_T = \left(\frac{\partial P}{\partial T}\right)_E$ derived from the coefficient relations under adiabaticity, i.e., the pyroelectric coefficient is directly connected to the entropy changes under applied field. The pyroelectric coefficient data, which was calculated from P-E loops captured at several temperatures ranging from 0°C to 90°C in increments of 5°C, was linearly interpolated on a grid of T and E values investigated in this study to consider its dependence on these parameters.

To understand the impact of texture on the direct ECE of the compositions of interest in this work, we have also carried out an analysis via the Landau theory of phase transitions. This would provide the primary ECE response expected from the changes of the order parameter of the system, namely electric polarization. We started off by writing Landau potential of the system in terms of the polarization components and their relative directions with respect to an applied field, $G(P_i, c, T, |\vec{E}|, \varphi, \theta)$ (Heitmann & Rossetti, J. Am. Ceram. Soc. 97, 1661–1685 (2014)):

$$G = \frac{1}{2}A_1(c,T)(P_1^2+P_2^2+P_3^2) + \frac{1}{4}B_1(c)(P_1^2+P_2^2+P_3^2)^2 + \frac{1}{6}C_1(P_1^2+P_2^2+P_3^2)^3$$
$$+\frac{1}{4}B_2(c,T)(P_1^4+P_2^4+P_3^4) + \frac{1}{6}C_2(P_1^6+P_2^6+P_3^6) + \frac{1}{6}C_3(P_1^2P_2^2P_3^2)$$
$$-E_1(|\vec{E}|,\varphi,\theta)P_1 - E_2(|\vec{E}|,\varphi,\theta)P_2 - E_3(|\vec{E}|,\varphi)P_3 \quad (2)$$

where c: composition, T : temperature, P_i: polarization components and $\vec{E}$: electric field vector, defined in spherical coordinates by its magnitude $|\vec{E}|$, polar angle φ and azimuthal angle θ and thus with components $E_1 = |\vec{E}|sin\varphi cos\theta$, $E_2 = |\vec{E}|sin\varphi sin\theta$, $E_3 = |\vec{E}|cos\varphi$ shown in Figure 15.

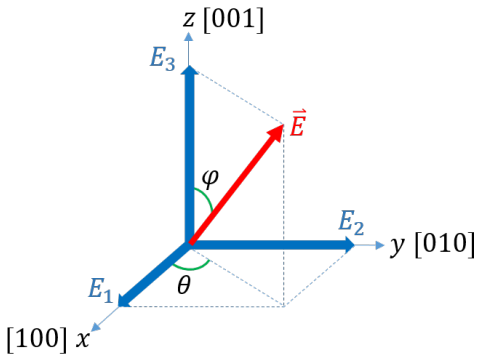

Figure 15. Electric field vector defined in spherical coordinates.

The coefficients used in our calculations are compiled from Heitmann & Rossetti, J. Am. Ceram. Soc. 97, 1661–1685 (2014) and Khakpash, N., Khassaf, H., Rossetti, G. A., and Alpay, S. P., Appl. Phys. Lett. 106, 082905 (2015) and are:

$$A_1(c,T) = [7.95 \times 10^5(1-c) + 3.15 \times 10^5 c][T - (748(1-c) + 262c)]$$

$$B_1(c) = 6.78 \times 10^8(1-c) - 1.17 \times 10^8 c$$

$$B_2(c,T) = 1.38 \times 10^9(c-0.7) - 1.51 \times 10^5[T - (748(1-c) + 262c)]$$

$$C_1 = 1.39 \times 10^9$$

$$C_2 = 1.54 \times 10^8$$

$$C_3 = -4.63 \times 10^8$$

Equations of equilibrium that relate the polarization components to electric field components are obtained by taking partial derivatives of G with respect to components of P:

$$\frac{\partial G}{\partial P_i} = A_1 P_i + B_1 P_i P_s^2 + C_1 P_i P_s^4 + B_2 P_i^3 + C_2 P_i^5 + \frac{1}{3} C_3 P_i \prod_{j=1, j\neq i}^{3} P_j^2 - E_i = 0 \qquad (3)$$

Simultaneous solution of these equations gives equilibrium polarization components, P_i, that yields the magnitude of polarization $P_s = \sqrt{\sum_{i=1}^{3} P_i^2}$ whose variation with respect to temperature, i. e the pyroelectric coefficient of PMN-PT, $\frac{\partial P_s}{\partial T}$, can be calculated and plugged into the ΔT expression for the ECE provided in Eq. (1). ΔT is computed using the Volterra evaluation of Eq. (1) and is therefore found numerically. In order to compute ΔT for a given composition for various

field directions at a given temperature, the entire range of polar angle φ (0-90 degrees) and azimuthal angle θ (0-45 degrees) were scanned in steps of 5 degrees, giving a total number of directions amounting to 172. The applied electric field was varied from 0 to 50 kV/m in steps of 1 kV/m and the ΔT was computed for each of these steps at a temperature range 0-700K. The resultant generated data is displayed in various forms along with their discussion in the next section.

4.1.Discussion of the response of the electrocaloric response of the PMN-PT system

Using the methodology prescribed in the previous section, we computed the ECE response of PMN-PT compositions starting from the 60/40 which is the tetragonal side of the MPB down to 90/10 and provide the results. The results plotted and discussed in the forthgoing section are for the max. of the EC induced ΔT that correspond to the temperatures just below the ferroelectric-paraelectric transition as provided in the Table 1.

Table 1. The ferroelectric-paraelectric transition temperatures for the $xPb(Mg_{1/3}Nb_{2/3})O_3$-(1-x)$PbTiO_3$ compositions studied in this work. Upper row: composition (in terms of x), lower row: Transition temperature (°C).

x	0.9	0.85	0.8	0.75	0.7	0.68	0.66	0.64	0.62	0.6
T_C (°C)	35	55	84	110	134	144	154	163	174	184

For all the direction dependencies of the compositions reported herein when computing the ECE, the relation between the field direction and the cubic perovskite crystal axis can be deduced from Figure 1. We specifically pick 6 compositions near the MPB where x ranges from 0.7 to 0.6. Part of our focus being centered on the compositions near the MPB is based on the conjecture that weakened polarization anisotropy could allow for ΔT changes in addition to the rhombohedral (r-phase) to tetragonal (t-phase) transition at the MPB. The MPB compositions are also thought to reflect the effect of the phase on the ECE for the PMN-PT system when a transition from the r-phase to the t-phase occurs. We find it very important here to state that all calculations started from a ground state in the compositions without any a priori assumption of the phase. The stable phases are thus computed from the thermodynamic parameters at zero field and compared to experimental data to ensure the correctness of the approach. Moreover, the rotation of the polarization upon application of a field along any of the 172 directions considered in both the r- and t-phases are computed at increments of the applied field. To accord with experiments, we assume that structural

variants do not form, meaning that the material remains in its initial single domain state, albeit distorted, throughout the application of the electric field. Such rotations do not necessarily correspond to those that approach a given field direction directly but a rather complicated trajectory following local minima in the energy landscape can arise as we show in the Supplementary Material. The computed ΔT values along different directions for all compositions already account for this phenomenon.

We first provide the ΔT variation as a function of applied electric field direction for the PMN-PT 60/40 in Figure 3, whose ground state is the t-phase and constitutes "the lower bound of the MPB" in the temperature-composition phase diagram [1]. A profound anisotropic dependence of ΔT on field orientation for the electric field amplitudes considered here is visible, evidenced by the distinct cupola-like topology along the major crystal axes. Interestingly, an identical trend was reported for the $BaTiO_3$ crystal in a DFT based effective Hamiltonian study near its tetragonal-to-paraelectric transition with the field along the [001] generating ΔT > ΔT [011] > ΔT [111] [2] agreeing with our results for the t-phase PMN-PT 60/40 composition. In Figure 16, a max. ΔT reaching around a value of 3.9°C appears possible if the field direction is close to the [112] crystal axis (denoted by the dark dashed lines), which does not coincide with the ground state polarization vector. Moreover, fields acting along one of the positively indexed <100> directions will also yield a lower ΔT, pointing out to the importance of the choice of texturing in these systems to maximize ECE. Note that the topology remains almost unchanged with increasing of the applied field amplitude.

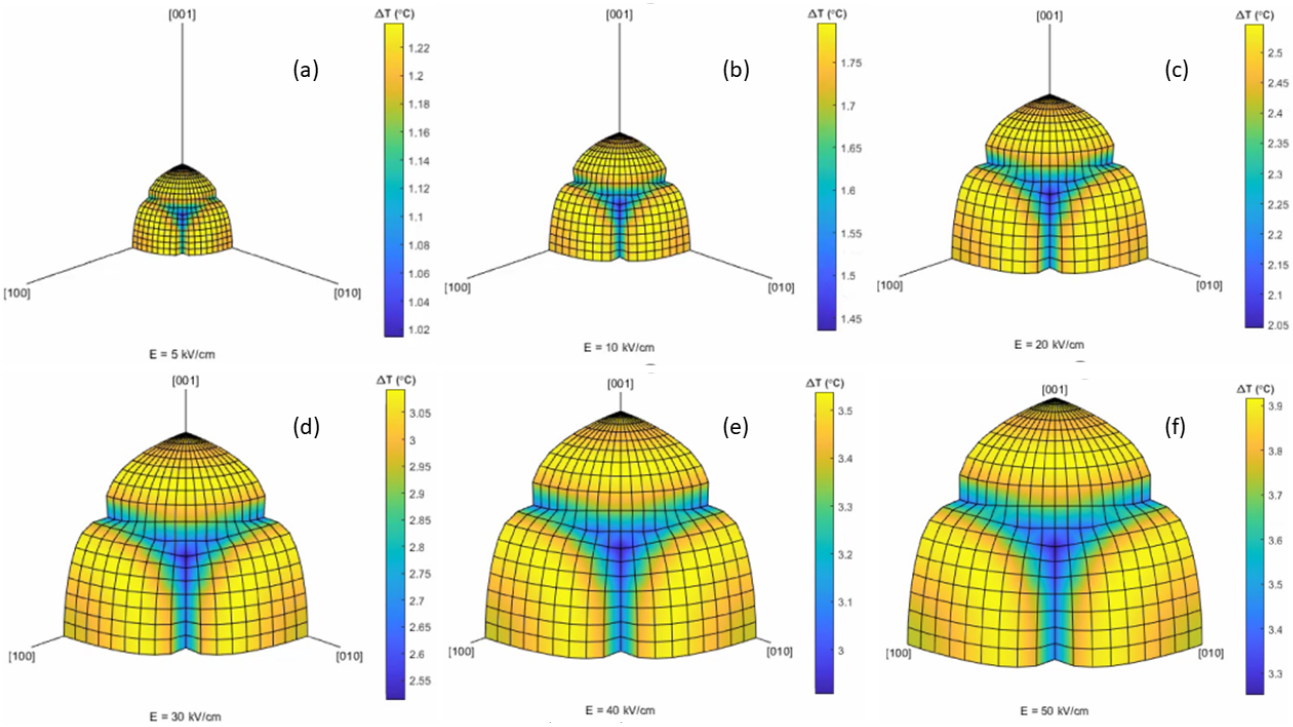

Figure 16. ΔT vs field orientation surface maps for PMN-PT 60/40 at the temperature where ΔT is maximal for a) 5 kV/cm, b) 10 kV/cm, c) 20 kV/cm, d) 30 kV/cm, e) 40 kV/cm and e) 50 kV/cm applied field values computed for 172 different directions.

We repeated the computation as a function of field orientation for the PMN-PT 70/30 the results of which are given in Figure 4. Chukka et al. have experimentally estimated, using the indirect approach, a ΔT value of 2.7°C for this composition in single crystal form at 127°C from temperature dependent hysteresis measurements having a max. field of 12 kV/cm along the [100] direction close to the transition temperature of 134°C [3]. This composition is the "upper bound of the MPB" and is in the r-phase in all the temperature range up to its respective Curie temperature (Tc). The analysis of the ΔT vs. applied field maps resulted in a distinctly different spherical topology in comparison to the PMN-PT 60/40 in Figure 16. Moreover, the ΔT values are also about 40-50% lower than that of the PMN-PT 60/40 for electric fields greater than 20 kV/cm in particular, implying the dramatic effect of the phase type on the ECE. In Figure 17, the maximum ΔT is achievable along the [111] direction that coincides with the spontaneous polarization direction in this composition, in stark contrast with what we compute for the t-phase. Like the PMN-PT 60/40 composition, the topology remains almost unchanged with applied electric field amplitude.

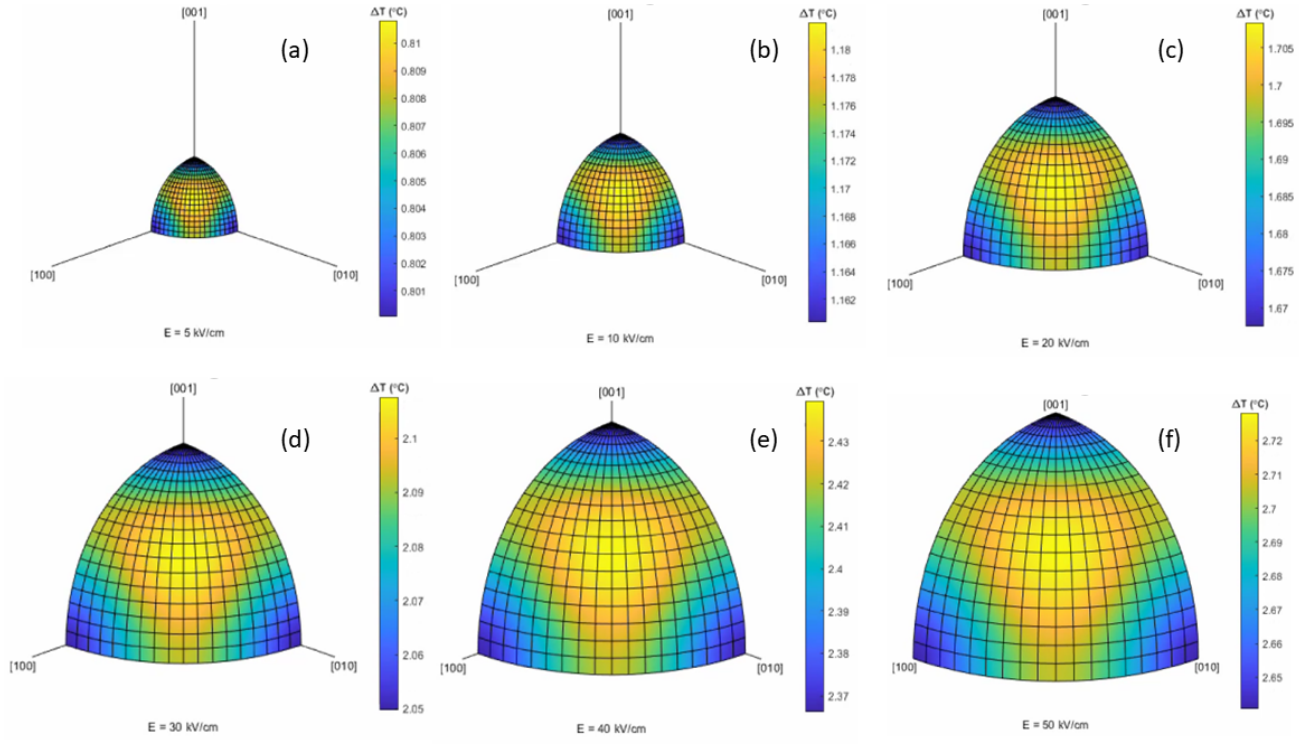

Figure 17. ΔT vs field orientation for PMN-PT 70/30 for a) 5 kV/cm, b) 10 kV/cm, c) 20 kV/cm, d) 30 kV/cm, e) 40 kV/cm and f) 50 kV/cm applied field values in 172 directions.

From a general perspective, one can infer that the t-phase displays higher ΔT values than the r-phase near the respective T_c's where maximal ΔT are reached. In connection with entropy changes under applied field, this is a somewhat counterintuitive outcome given that r-phase compositions near the upper bound of the MPB are expected to exhibit a weaker anisotropy, meaning that the relative ease with which the polarization can rotate could be expected to allow for larger entropic changes under an increasing applied field. In fact, in general, for the compositions in the vicinity of the MPB, the overall ΔT values of the t-phase, despite the slightly stronger anisotropy, are higher than the r-phase compositions. For compositions falling between the 70/30 and 60/40 that intersect the MPB line in the PMN-PT phase diagram, a gradual change in topology occurs upon transitioning from the r-phase to the t-phase at the respective temperatures where maximal ΔT is achieved for 50 kV/cm applied field, which is displayed in Figure 18.

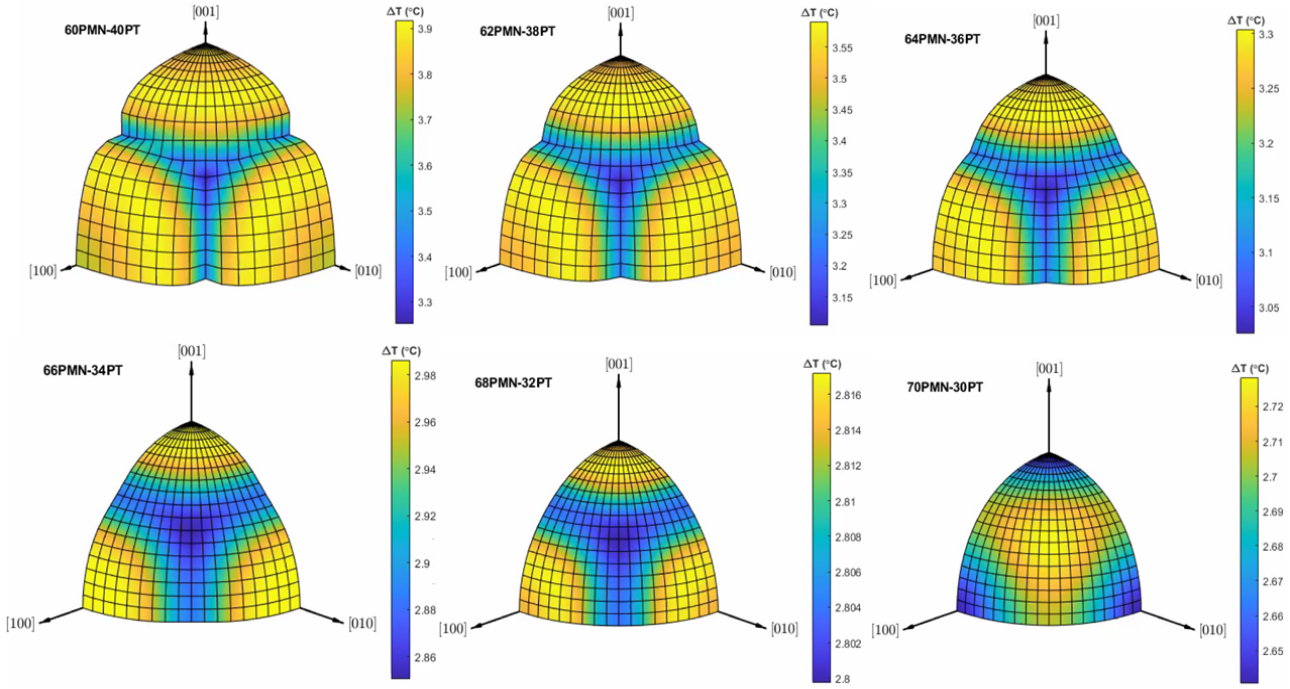

Figure 18. Change of ΔT surface topology for compositions near the MPB (going from tetragonal PMN-PT 60/40 to the rhombohedral PMN-PT 70/30 composition) for an applied electric field of 50 kV/cm. Notice the change in directionality of the maximal ΔT from the tetragonal phase to the rhombohedral phase.

Specifically, the ferroelectric state switches from the t-phase to r-phase when going from the PMN-PT 68/32 to the PMN-PT 70/30 composition at which an abrupt, visible change of direction of maximal ΔT occurs whereas the topology only slightly changes (See Figure 18). Phase transition temperatures of the former and latter are approx. 130°C and 120°C respectively. As the two compositions are in the immediate vicinity of the MPB boundary near their respective T_c's, a rather weak dependence on direction is expected due to lower anisotropy energy cost in both compositions, keeping the topology almost constant. The distinct difference between the r-phase ECE and t-phase ECE is therefore visible for the PMN-PT 70/30 and PMN-PT 60/40 comparison given in Figure 18 in spite of the fact that all results are obtained near the respective transition temperatures (See Table 1). Therefore, given that the t-phase compositions have higher polarization amplitudes, it can be argued that the amplitude of polarization is a more prominent parameter for the ECE than the ease with which it can rotate to achieve maximal ΔT. It is also interesting to note that a 10% alteration of the solid solution composition towards the t-phase yields

about a 30% enhancement in the ECE effect upon a transition to the t-phase from the r-phase for the maximal field of 50 kV/cm. Going beyond the near-MPB compositions towards the PMN-rich range, we notice that the field orientation of the ΔT values start to deviate from the [111] direction in a gradual manner. One such example is the PMN-PT 80/20 composition whose applied field orientation vs. ΔT surfaces are provided in Figure 19.

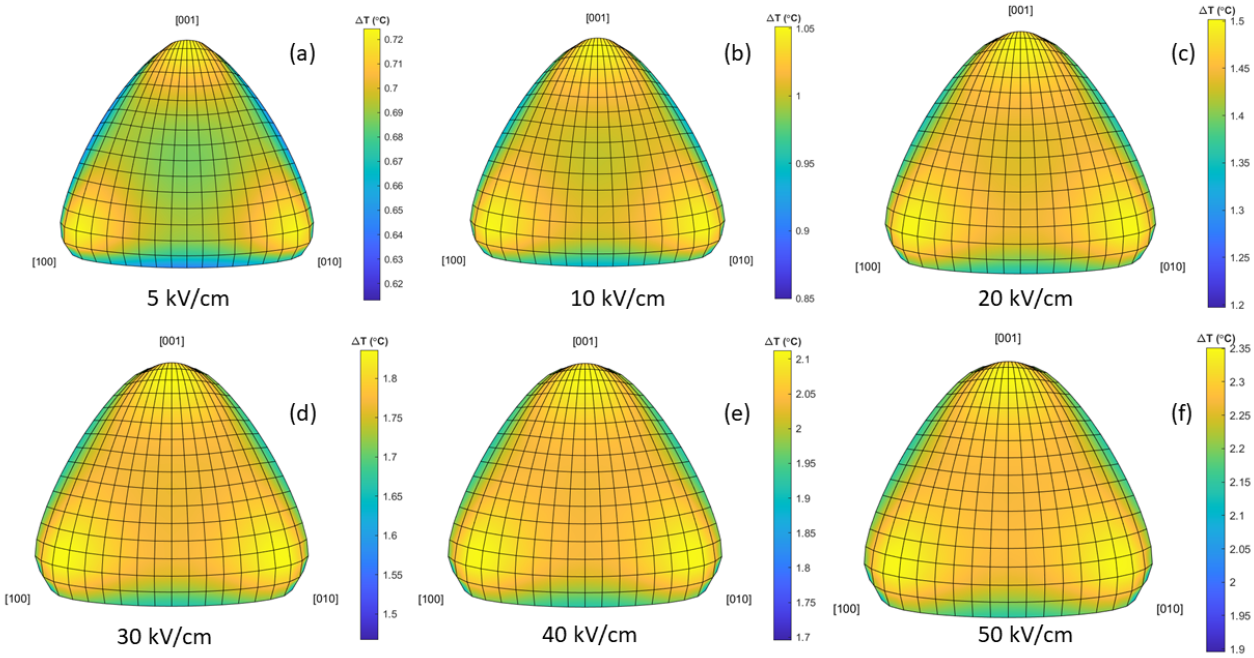

Figure 19. ΔT vs field orientation for PMN-PT 80/20 for a) 5 kV/cm, b) 10 kV/cm, c) 20 kV/cm, d) 30 kV/cm, e) 40 kV/cm and e) 50 kV/cm applied field values in 172 directions.

Directional dependency of the max. ΔT for the PMN-PT 80/20, while differing from the PMN-PT 70/30 composition, clearly shifts towards one of the [100], [010] or [001] axes, albeit not parallel. The maximal value of ΔT is also reduced, likely due to the lessened contribution of the coefficients in the energy potential favoring ferroelectricity. Increasing the PMN content further to 90% in the PMN-PT solid solution retains the r-phase with the ground state polarization vector pointing along the [111] direction, however the maximal values of ΔT are obtained if the electric field is applied along any one of the [100], [010] or [001] axes as displayed in Figure 20. Compared to the PMN-PT 70/30 and PMN-PT 80/20 compositions that are also in the r-phase, this is a striking difference. This outcome is explainable based on our earlier argument that it is the amplitude of polarization near the temperature of maximal ΔT rather than the ease with which it rotates: The PMN-PT 90/10 composition exhibits a weaker polarization before transitioning into the paraelectric phase than

that of the PMN-PT 70/30. Such dependence of the ECE on composition near the transition temperatures accords very well with the experimental reports for powder samples [4].

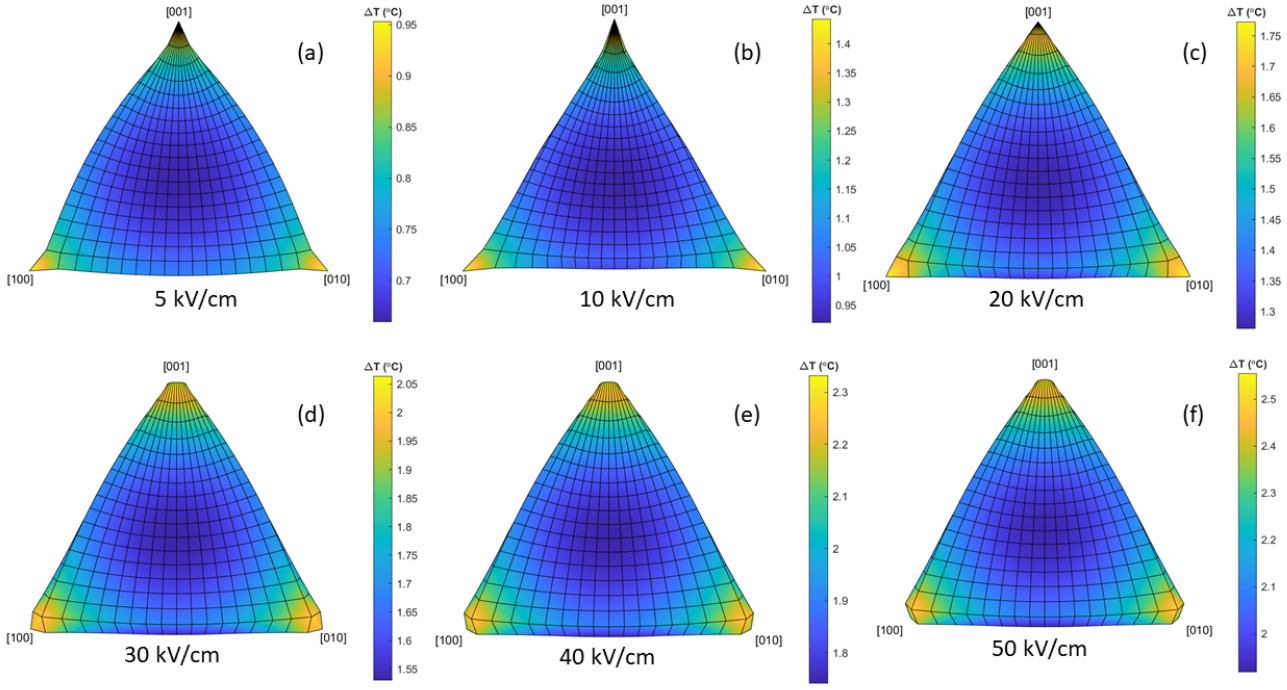

Figure 20. ΔT vs field orientation for PMN-PT 90/10 for a) 5 kV/cm, b) 10 kV/cm, c) 20 kV/cm, d) 30 kV/cm, e) 40 kV/cm and e) 50 kV/cm applied field values in 172 directions.

We finally compare the ΔT vs field orientation topologies at a max. electric field of 50 kV/cm in Figure 21. There is a distinctive shift of the crystal axes from around the [111] direction towards any one of the [100], [010] or [001] axes along which maximal ΔT is obtained. While this occurs, it is worth noting that the maximal value of ΔT does not differ substantially but with the interesting outcome that the [111] axes along which maximal ΔT is possible in the 75/25 composition becomes the direction where the minimum

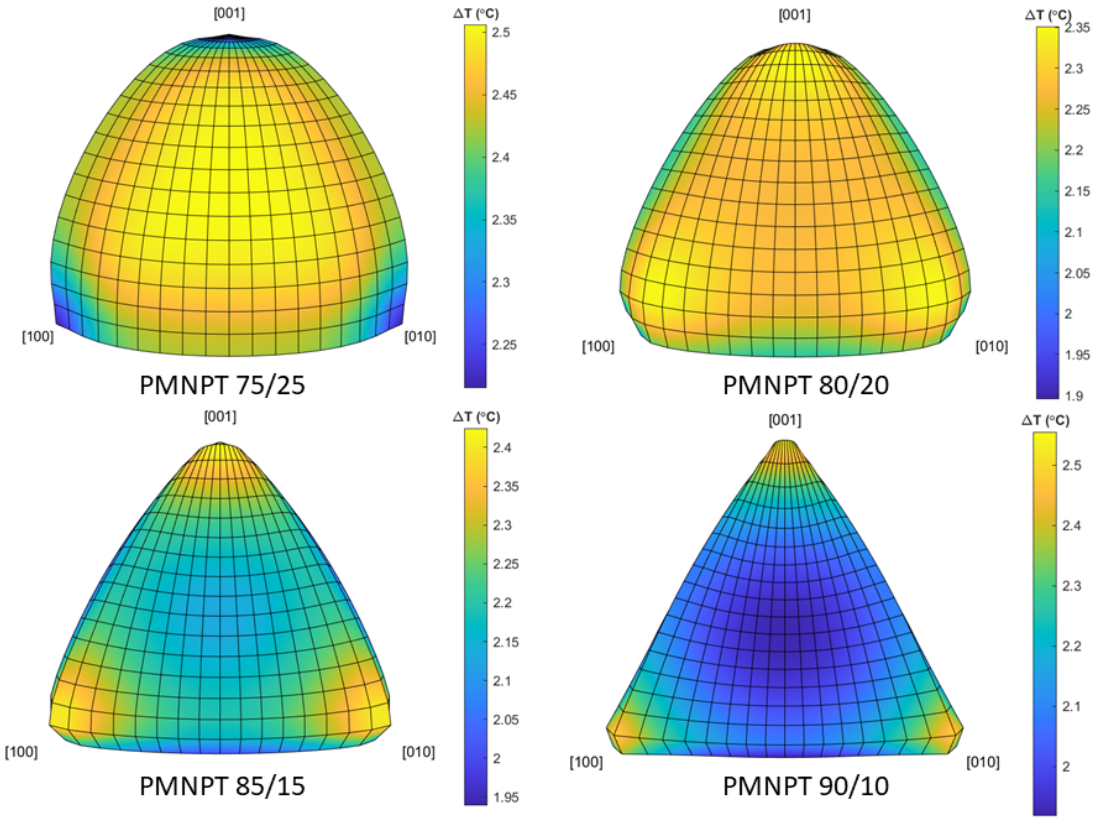

Figure 21. Change of ΔT surface topology for compositions in the PMN rich compositions in PMN-PT for an applied electric field of 50 kV/cm. Notice the change in directionality of the maximal ΔT with composition despite all being in the r-phase in the ground state.

ΔT is exhibited in the 90/10 composition. This is even though both compositions are in the same r-phase. Therefore, apart from the choice of the composition being an obvious parameter in an ECE application, one should also expect dramatic variations in the orientational dependence of the ECE in a rather counter-intuitive manner rendering the computation of the anisotropy dependence an important requirement for any choice of composition. As a final note, we would like to remind that the ΔT values computed in the current work refer to the maximum ΔT values that are attainable at temperatures close to the T_c. Since possible ECE devices are expected to operate in a certain temperature range which may not directly match with the T_c of the system, the ΔT values that are attainable in the operational temperature range should be considered, in addition to the observed anisotropy of the system.

Experimental measurements on the anisotropy of the ECE in bulk perovskite oxides are rare, let alone the PMN-PT system. The measurements on the PMN-PT 76/24 composition in Ref. [5] yield identical values for ΔT when the fields are applied along [100] and [110] while an enhancement is observed for ΔT when the field is applied along the [111] direction that is qualitatively in agreement with the results we obtain for the PMN-PT 75/25 composition. Similar results were also reported by Sebald and co-workers where the maximal heat release was recorded for when the applied field acted along the [111] direction in the same material [6]. Note that the values in Refs. [20] and [21] are considerably lower than that of reported in [3], an outcome not explainable on the basis of the 4-5% PMN composition difference aside from the low values of the field applied in [29]. Direct measurements on ΔT in Ref. [7] on <011> oriented crystals in PMN-PT 72/28 have yielded values of 0.53°C at 9 kV/cm field near the transition temperature (~130°C), almost half of what we estimate from our calculations for the orientation of interest in that work. From the foregoing discussion, we argue that elastocaloric effects due to the volume changes are partly responsible for this systematic discrepancy between single crystal calculations and direct measurements. A composition based systematic study was that of Peräntie et al. [4] reporting direct measurements on a wide range of PMN-PT compositions but in the polycrystalline form. Polycrystalline sample results in Ref [4], albeit not comparable with single crystal data, still provides a guide to reflect on our findings. The increase in ΔT for all the field magnitudes with increasing of the PT content near the transition is in full qualitative agreement with what we here predict. ΔT values measured therein near the respective transition temperatures (beyond which the energy potential in our work does not apply) are roughly about half of the arithmetic averages of the ranges we computed in our work for a given composition. The adiabatic volumetric strain in a single PMN-PT crystal is estimated (See the Appendix) to be capable of causing temperature changes of around -1°C or more at 50 kV/cm, namely the elastocaloric effect. In fact, depending on the variations in the piezoelectric coefficients as a function of composition and temperature favoring volumetric expansion under the action of an applied field, this value can exceed -1°C (in the negative direction) or approach 0K, resulting in reduction of the overall caloric response. This implies that elastocaloric phenomena can be a factor in the apparent deviation of the values we compute for the ECE from the values measured in experiments on the polycrystalline samples. Moreover, as some crystallites or domains can possess polar axis close to an antiparallel state with respect to the global field coordinate, negative ΔT response may emanate as demonstrated in Ref.

[8] for Ba,Sr,TiO_3 and reducing the overall caloric effect, as also discussed in a recent work [9]. The anomaly of the heat capacity near the transition could be thought of as another factor but the electric fields will smear it, connecting the reduced ΔT to heat capacity anomalies an almost obsolete argument. Despite this, the ΔT surfaces computed herein are expected to serve as a valuable guide in designing energy efficient and effective ECE based thermal management devices based on PMN-PT or similar solid solutions.

In the course of the work whose details are laid above, the following question arose: Do the strains induced under an applied electric field cause temperature change? This is a very appropriate and valid question for the systems analyzed in this project owing to the piezoelectric nature of the PMN-PT system. It is very well known from thermodynamics that any material undergoing volume changes in the presence of an external field will exhibit entropy changes due to change in volume. Bearing in mind this fact, we went on to carry out and analysis of this effect and estimate a formulation to reveal the temperature changes possible for a free-standing single ferroelectric crystal as the following: The analysis is based on the temperature change because of the volume change emanating from the converse piezoelectric effect, i. e. the deformation induced in the crystal because of applied electric field.
Reverse piezoelectric relation can be written as

$$\epsilon_{jk} = d_{ijk}E_i \tag{4}$$

with ϵ_{jk} being the components of the strain tensor, d_{ij} are the converse piezoelectric tensor elements E_i are the field components that are oriented parallel to the polar axis. In matrix representation it reduces to;

$$\epsilon_j = d_{ij}E_i \tag{5}$$

Considering the 3m and 4mm point group crystals (See [10]), molar volume change can be approximated by;

$$\Delta V \approx (\epsilon_1 + \epsilon_2 + \epsilon_3) \cdot V_i \tag{6}$$

where V_i is initial (under zero field) molar volume at arbitrary temperature and $\epsilon_1 + \epsilon_2 + \epsilon_3$ are normal strain components. From Eq.**Hata! Başvuru kaynağı bulunamadı.Hata! Başvuru**

kaynağı bulunamadı. Hata! Başvuru kaynağı bulunamadı.Hata! Başvuru kaynağı bulunamadı.Hata! Başvuru kaynağı bulunamadı.Hata! Başvuru kaynağı bulunamadı.5 electric field induced strains due to the piezoelectric effect can be written as;

$$\begin{aligned} \epsilon_1^p &= d_{31} \cdot E_3 \\ \epsilon_2^p &= d_{31} \cdot E_3 \\ \epsilon_3^p &= d_{33} \cdot E_3 \end{aligned} \tag{7}$$

for the 4mm point group and;

$$\begin{aligned} \epsilon_1^p &= d_{31} \cdot E_3 - d_{21} \cdot E_2 \\ \epsilon_2^p &= d_{31} \cdot E_3 + d_{21} \cdot E_2 \\ \epsilon_3^p &= d_{33} \cdot E_3 \end{aligned} \tag{8}$$

for the 3m point group. Including the Poisson effect, the above expression becomes;

$$\begin{aligned} \epsilon_1 &= \epsilon_1^p - \nu(\epsilon_2^p + \epsilon_3^p) \\ \epsilon_2 &= \epsilon_2^p - \nu(\epsilon_1^p + \epsilon_3^p) \\ \epsilon_3 &= \epsilon_3^p - \nu(\epsilon_1^p + \epsilon_2^p) \end{aligned} \tag{9}$$

with ν being the Poisson ratio. Considering the relation

$$\epsilon_1^p + \epsilon_2^p + \epsilon_3^p = (2d_{31} + d_{33}) \cdot E_3 \tag{10}$$

the total linear strain then becomes

$$\epsilon_1 + \epsilon_2 + \epsilon_3 = (2d_{31} + d_{33})(1 - 2\nu) \cdot E_3 \tag{11}$$

where E is given in units of kV/cm. Then molar volume change can be calculated as

$$\Delta V \approx (\epsilon_1 + \epsilon_2 + \epsilon_3) \cdot V_i = (2d_{31} + d_{33})(1 - 2\nu)V_i \cdot E_3 \tag{12}$$

4.2.Adiabatic Temperature Change as a Function of Volume

Now that we have the expression for volume change under an electric field, we can go ahead and write temperature under constant electric field as;

$$T = T(S, V, n) \tag{13}$$

since S and n are constant one can write;

$$dT = \left(\frac{\partial T}{\partial V}\right)_S dV \tag{14}$$

to find the partial derivative one can written as;

$$\begin{gathered}\left(\frac{\partial T}{\partial V}\right)_S \cdot \left(\frac{\partial S}{\partial T}\right)_V \cdot \left(\frac{\partial V}{\partial S}\right)_T = -1 \\ \left(\frac{\partial T}{\partial V}\right)_S \cdot \frac{C_V}{T} \cdot \left(\frac{\partial V}{\partial S}\right)_T = -1\end{gathered} \tag{15}$$

and from Maxwell relations;

$$\left(\frac{\partial S}{\partial V}\right)_T = \frac{\alpha}{\beta_T} \tag{16}$$

where α is the thermal expansion coefficient and β_T is isothermal compressibility. Eq. 16 then becomes;

$$\left(\frac{\partial T}{\partial V}\right)_S \cdot \frac{C_V}{T} \cdot \frac{\beta_T}{\alpha} = -1 \tag{17}$$

hence;

$$\left(\frac{\partial T}{\partial V}\right)_S = \frac{-\alpha T}{C_V \beta_T} \tag{18}$$

Finally, adiabatic temperature change in terms of volume can be written as;

$$dT = \frac{-\alpha T}{C_V \beta_T} dV \tag{19}$$

re-arranging gives;

$$d\ln T = \frac{-\alpha}{C_V \beta_T} dV \tag{20}$$

and assuming material properties are constant, one can find

$$T_f = T_i \cdot \exp\left(\frac{-\alpha}{C_V \beta_T} \cdot \Delta V\right) \tag{21}$$

Inserting $\Delta V \approx (\epsilon_1 + \epsilon_2 + \epsilon_3) \cdot V_i = (2d_{31} + d_{33})(1 - 2\nu)V_i \cdot E_3$ into the relation above yields

$$T_f = T_i \cdot exp\left[\frac{-(2d_{31} + d_{33})(1 - 2\nu)V_i \alpha}{C_V \beta_T} \cdot E_3\right] \tag{22}$$

Subtracting T_i from both sides yields ΔT which is what we seek to find for "volume change induced temperature change" namely the elastocaloric effect;

$$\Delta T = T_i \cdot \left[exp\left(\frac{-(2d_{31} + d_{33})(1 - 2\nu)V_i \alpha}{C_V \beta_T} \cdot E_3\right) - 1\right] \tag{23}$$

In Eq. 23 above, note that E_3 is in kV/cm and is selected to be always zero, and, C_V and V_i are molar properties. Given that $2d_{31} + d_{33} > 0$ and other thermodynamic parameters in A20 are also grater then zero and that $\nu < 0.5$ always (See Refs. [11-16] from which the constants were compiled to carry out the estimation formulated herein) makes the exponent term in (23) smaller then unity, which yields $\Delta T < 0$. Hence it is likely that elastocaloric and electrocaloric effects are competing quantities in an experiment, and the elastocaloric effect for the PMN-PT is thus shown to yield $\Delta T < 0$ for $\Delta V > 0$ when applied field is directed along or close to the polar axis.

5. Effect of point defect on the properties of the chosen system: La-doping effects in PZT 70/30

Main question: How does the electrical and ECE properties changes by a doping material?

Solution approach: A prototype system was chosen. Then computational analyses were conducted by creating defects in the structure.

Part of the project proposal was about the study of dopant type defects on the ECE of ferroelectric perovskite solid solutions. To serve this purpose, we developed simulations study that incorporate the effects of La in the PZT 70/30 lattice as defects sites in parallel with the experimental work. Given that the maximum ECE is achievable near the ferroelectric-paraelectric transition temperature where the pyroelectric coefficients reach maximal values, ferroelectric perovskite compositions whose Curie temperatures can be varied via doping that generate systematic changes in A-site or B-site elements are specifically attractive as they allow tuning of the ECE for the temperature of the desired operational range. Among such PZT based compositions, La-doped PZT (PLZT) is a well-known perovskite with prominent ferroelectric and electro-optic properties. Systematic doping of lanthanum (La) to the A-site position of the perovskite PZT strongly affects the electrical properties. The $(Pb_{1-x}\ La_x)(Zr_{0.65}\ Ti_{0.35})$, known in short as x/65/35, are the most studied compositions due to their vicinity to the morphotropic phase boundary (MPB) [17, 18]. The x/70/30 is a less studied composition with very few reports in the literature including thin films near the MPB [19-21] shifting our focus to the properties of this system in this work. This composition also sits at a location where the near morphotropic compositions gradually shift towards Zr-rich AFE ones [22]**.** That the PLZT 70/30 composition is claimed to exhibit FE_R, SFE and AFE phases as well as a mix of these with varying La content motivated us to synthesize PZT 70/30 in a wide range of La doping followed by structural and electrical characterization Recent studies have focused on polar nanoregions (PNRs) and their effect on ECE as PNRs were claimed to enhance the ECE through possession of multiple orientation possibilities, which is ultimately connected to variations in dipolar entropy when acted upon by an external field [19, 23, 24]. Motivated by the above findings and claims, $(Pb_{1-x}La_x)(Zr_{0.70}Ti_{0.30})$ with x/70/30 ceramics (x=0.05-0.12) were investigated for their ECE performance in this study. The data obtained were discussed with a focus on the nature of the ferroelectric character of the compositions, i. e. whether it is a normal ferroelectric, antiferroelectric or relaxor ferroelectric character. In parallel with experiments, incorporation of La as point defects in a ferroelectric lattice was computationally

simulated using the Landau-Devonshire-Ginzburg phenomenology in a 2D lattice. The strain and electrostatic fields associated with La sites generate a highly inhomogeneous lattice resembling that of a relaxor composition. Our experimental results can be explained on basis that La doping introduces donor/acceptor point defect centers into the lattice likely forming defect-dipole complexes, shifting a major portion of our focus to this phenomenon. Defect-dipole complexes and their effects on crystal properties have been a topic in several theoretical and experimental works [25-28]. The consideration of a defect dipole model in our work explains very well the progressive slanting of the hysteresis with increasing La content at room temperature (RT) in addition to lowering of the transition temperature accompanied by a strong smearing of the dielectric anomaly, indicative of the highly inhomogeneous lattice strains and local fields. This outcome tempts us to question the AFE nature of the composition of interest herein claimed in several works [22, 29]. Within this picture, there exists a critical La composition that yields a pronounced increase in the EC driven dT change persisting in a wide temperature range that fall on the ferroelectric side of the polar - nonpolar transition. The very same outcome supports our hypothesis that question the possible coexistence of the AFE phase: the effect of an AFE phase was recently reported [30] to drive a negative pyroelectric coefficient in stark contrast with the result we hereby report. We further discuss our results in the light of the above arguments as well as theory of inhomogeneous transitions. There is strong evidence that La doping of the PZT 70/30 can stabilize an AFE phase coexisting with an FE order. On the other hand, approximately 8.7 % ionic radius misfit between Pb and La can generate local strains in the PZT30/70 lattice in addition to the dipolar complexes that form because of the charge imbalance when Pb is replaced with La. It is well known that presence of such defects in a FE lattice is expected to influence properties and impact FE stability without any need to resort to AFE phase formation and other mechanisms alike. To acquire an understanding of the impact of the types of defect complexes, we are in the process of adapting a Landau-Ginzburg-like formalism to shed light on defect-driven effects in a model perovskite system such as the PZT compositions. The calculations were done on a 100 x 100 nm 2D grid with a random distribution of defect sites representing the La dopants. We assumed that these sites generate displacements on the nearest neighbor sites of amplitude ½ ($D_{Pb} - D_{La}$) along both the vertical and horizontal reference axes where D stands for the ionic radius of Pb and La in the 12-coordination state. For a schematic, please refer to Figure 22.

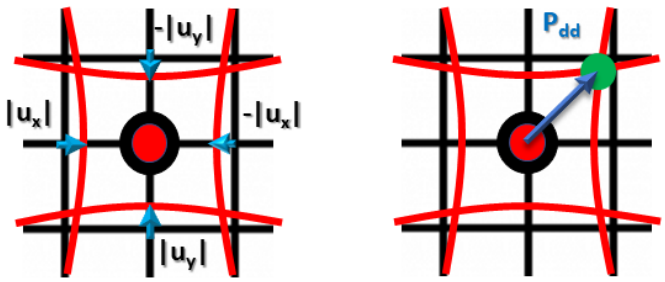

Figure 22. Left: Schematic of a La ion (red ball) replacing the Pb site (black ball), causing a local distortion represented here by the red lines (black lines indicate the defect- and strain-free lattice) where the displacements, ui, along y- and x-axis are given as blue arrows. |ui| denote the amplitude of the displacement. Right: A defect dipole inducing a fixed polarization due to the charge imbalance generated upon replacement of the Pb with La.

In this case, we are not interested in anisotropy effects and fix a cartesian coordinate taking a cubic lattice as reference where the axes consist of the [001], [010] and [100] directions respectively. The free energy of such a system in 2D (assuming that the system is infinite in the 3rd dimension) can be written as:

$$F = \alpha(P_1^2 + P_3^2) + \beta(P_1^4 + P_3^4) + \gamma(P_1^6 + P_3^6) + \alpha' P_1^2 P_3^2 + \beta'(P_1^2 P_3^4 + P_1^4 P_3^2) + r_1(u_{11}P_1^2 + u_{33}P_3^2) + r_2(u_{11}P_3^2 + u_{33}P_1^2) + r_4 u_{33} P_1 P_3$$
$$+\frac{1}{2} c_{11}(u_{11}^2 + u_{33}^2) + c_{12}u_{11}u_{33} + c_{44}u_{11}u_{33} + \partial\left(dP_{1,1}^2 + dP_{1,3}^2 + dP_{3,1}^2 + dP_{3,3}^2\right) \quad (24)$$

where α, β, γ, α', β' are the phenomenological coefficients of PZT 70/30, r_1, r_2 and r_4 are the coefficients that couple the strains, u_{11} and u_{33}, to polarization components P_1 and P_3, c_{ij} are the elastic stiffness constants at constant polarization, ∂ is the coefficient of gradient energy (assumed isotropic here) and $dP_{i,j}^2$ represent the square of the derivative of a polarization component i along a direction j. The stresses in the system can be written as:

$$\sigma_{11} = c_{11}u_{11} + c_{12}(u_{22} + u_{33}) + r_1 P_1^2 + r_2 P_3^2 \quad (25a)$$

$$\sigma_{33} = c_{11}u_{33} + c_{12}(u_{11} + u_{22}) + r_1 P_3^2 + r_2 P_1^2 \quad (25b)$$

computed from the condition that

$$\frac{dF}{du_{ij}} = \sigma_{ij} \quad (26)$$

Components of the stress tensor σ_{ij} satisfy the mechanical equilibrium condition as:

$$\frac{\partial \sigma_{ij}}{dx_j} = 0 \tag{27}$$

The strains in 2a and 2b can be written in terms of the displacements using

$$u_{ij} = \frac{1}{2}\left(\frac{du_i}{dx_j} + \frac{du_j}{dx_i}\right) \tag{28}$$

where u_i are the displacement vector components in 2D. In order to simulate the effect of dopants on the grid, namely La sites generating local strains in the computational grid, a "background" displacement vector is assigned to the nearest neighbors of these sites whose value does not change any time, so $u_i(r) = u_i'(r) + u_{La}$ where u_i' is the displacement to be solved at every coordinate, *r*, while u_i^{La} are the displacements neighboring the La site along the i and j axis induced by the ionic misfit between La and Pb (See Figure 22). for the state of 12 coordination. La sites are distributed in the 2D grid with N sites randomly with the condition that

$$\frac{1}{N}\sum_{n=1}^{N} Cn = La_{Conc} \tag{29}$$

where C is either 1 or 0. Whether C is 0 or 1 is decided depending on a random number, λ, generated between 0 and 1 for every site is less than the max conc. of La chosen for the grid (which varies between 0 and a max. value of 0.05 in 2D for this work). For instance, $C = 1$ at site *ij* if $\lambda < La_{Conc}$ for that site or else $C = 0$. Such a procedure gives a random distribution of La sites whose average concentration does not exceed the desired value to be studied in each simulation run. Note that this does not mean the total displacement remains the same at these sites as there is a displacive component sensitive to electrostrictive effects induced by the polarization. The system also satisfies the Poisson equation:

$$\frac{dD_i}{dx_j} = \rho \tag{30}$$

where $D_i = \varepsilon_0 \varepsilon_b E_i + P_i$ is the dielectric displacement vector and ρ is charge that can vary as a function of position, ε_0 is the permittivity of vacuum, ε_b is the background dielectric constant of the ferroelectric, E_i is the electric field that can be expressed as the gradient of the electric potential, namely $E_i = -\frac{d\emptyset}{dx_i}$. Free energy has to be minimized variationally to obtain the relation between E_i and P_i as the following:

$$\frac{dF}{dP_1} - \frac{d}{dx_3}\left(\frac{dF}{df_1}\right) - \frac{d}{dx_1}\left(\frac{dF}{df_2}\right) = 0, \frac{dF}{dP_1} - \frac{d}{dx_3}\left(\frac{dF}{df_1}\right) - \frac{d}{dx_1}\left(\frac{dF}{df_2}\right) = 0 \tag{31}$$

with

$$f_1 = dP_3/dz,\ f_2 = dP_3/dx,\ f_3 = dP_1/dz \text{ and } f_4 = dP_1/dx \tag{32}$$

The relation between P_i and E_i are established through Eq. 8 and are solved simultaneously with Eqs. 4 and 7 from which $P_i(r)$, $u_i(r)$, $\varphi(r)$ are found using a numerical iterative scheme with a convergence criterion of 10^{-7} difference for P_i. Strains, u_{ij} (i, j = 1, 3), electric field components, E_i, can then be obtained.

When doped, there are two possible sites in the perovskite cell that a cation can occupy. In the case of PZT, the 12 coordinated A-site is occupied only by Pb^{2+} that has an ionic radius of 1.49 nm. The B-site position in the perovskite lattice, on the other hand, is occupied by the Zr^{4+} and Ti^{4+} cations. The B-site cation has octahedral coordination with six oxygen nearest neighbors. When the ionic radii of VI and XII coordinated La^{3+} are considered, it is obvious that La^{3+} would assume the A-site position replacing Pb^{2+} in the ABO_3 perovskite structure. However, this substitution would create charged point defects that would unavoidably affect the electrical properties. Possible scenarios on the defect chemistry of PLZT are considered below.

Scenario I: In lead-containing perovskites, the lead volatilization during the sintering process causes the formation of negatively charged Pb vacancies $[V''_{Pb}]$. Using Kröger-Vink notation positively charged oxygen vacancies $[V_O^{\bullet\bullet}]$ are also created to retain the charge neutrality according to the Eq (11):

$$\left(\mathrm{Pb}^{2+}_{\mathrm{Pb}^{2+}}\right)^{\times} + \left(\mathrm{O}^{2-}_{\mathrm{O}^{2-}}\right)^{\times} \leftrightarrow PbO \uparrow + [V''_{Pb}] + [V_O^{\bullet\bullet}] \tag{33}$$

Limited donor doping of La^{3+} in the A-site of the perovskite lattice in the form of La_2O_3 would decrease the concentration of the cation and anion vacancies, i. e. $[V''_{Pb}]$ and $[V_O^{\bullet\bullet}]$, that are already present in the solid according to the defect Eq (12):

$$La_2O_3 + [V''_{Pb}] + [V_O^{\bullet\bullet}] \leftrightarrow 2\left(\mathrm{La}^{3+}_{\mathrm{Pb}^{2+}}\right)^{\bullet} + 2\left(\mathrm{O}^{2-}_{O^{2-}}\right)^{\times} + \frac{1}{2}O_2(g) + 2e' \tag{34}$$

The positively charged defect $\left(\mathrm{La}^{3+}_{\mathrm{Pb}^{2+}}\right)^{\bullet}$ is compensated by two electrons (e') in the conduction band derived from the Ti 3d states, which would then lead to mobile point charges in the solid.

Scenario II : In some cases where the ceramics have already been sintered under a PbO rich atmosphere and the cation and anion vacancies are limited, or the amount of La^{3+} doping is done at higher ratios, then the positively charged defect $\left(La_{Pb^{2+}}^{3+}\right)^{\bullet}$ can be compensated by the creation of additional cation vacancies with one $[V_{Pb}'']$ being created for two $\left(La_{Pb^{2+}}^{3+}\right)^{\bullet}$ or one $[V_{Ti}'''']$ for four $\left(La_{Pb^{2+}}^{3+}\right)^{\bullet}$ following the defect Eqs. (13a) or (13b), respectively:

$$La_2O_3 \leftrightarrow 2\left(La_{Pb^{2+}}^{3+}\right)^{\bullet} + 2\left(O_{O^{2-}}^{2-}\right)^{\times} + [V_{Pb}''] + PbO \uparrow \quad (35a)$$

$$2La_2O_3 \leftrightarrow 4\left(La_{Pb^{2+}}^{3+}\right)^{\bullet} + 4\left(O_{O^{2-}}^{2-}\right)^{\times} + [V_{Ti}''''] + 'TiO_2' \quad (35b)$$

where $PbO \uparrow$ in Eq. (13a) means removal of lead oxide through evaporation, and $'TiO_2'$ in Eq. (35b) means segregation of titanium dioxide as a separate phase. Note that *scenario II* corresponds to the defect-dipole formation mechanism considered in the simulations prescribed in the previous section: La sites acting as donors whilst the Pb vacancies acting as acceptor sites has served as the basis of the simulation study in this work. Substitution of La^{3+} with an ionic radius of 1.360 Å to the A-site position replacing Pb^{2+} with an ionic radii of 1.490 Å would also lead to tensile stresses arising around the $\left(La_{Pb^{2+}}^{3+}\right)^{\bullet}$ defects. Absence of B-site cations, i. e. $[V_{Pb}'']$ or $[V_{Ti}'''']$ defects would also cause a similar tensile strain around their corresponding location. The effect of these strains on the electrical properties combined with the electrostatic effects has been the focus of our analyses of the simulation results. Owing to the approximately 8.7 % ionic radius misfit between Pb and La for 12 coordination, local strains in the PZT 30/70 lattice will be generated in addition to the dipolar complexes that form because of the charge imbalance when Pb is replaced with La. It is well known that presence of such defects in a FE lattice is expected to influence properties and impact FE stability without any need to resort to AFE phase formation and other mechanisms alike. Noticing that the microstructures of the samples are insensitive to the La doping levels with no verifiable changes in grain size or texture, changes in the hysteresis shapes and the reduction in the T_c along with the smearing of anomalies can be thought of as a direct consequence of the change of the inherent lattice properties upon La addition. To get a qualitative idea on the changes brought about when La dopants are introduced into the PZT 70/30 lattice, we followed the methodology prescribed to simulate these effects and compare the trends in our findings with experiment. In addition to local strain fields generated, the randomly distributed La-sites also are

considered to act as donors with neighboring acceptors to sustain charge neutrality, forming dipole-defect complexes.

Note that a gradual increase in La concentration associated with defect dipoles can rapidly degrade the hysteresis especially when approaching 8% considered in our simulations. This trend is qualitatively in very good agreement with trends of the experimental hysteresis despite that the simulation is carried for a single crystal 2D grid. A similar set of results were obtained by Pu et al. [28] where dramatic slanting of hysteresis were observed in oxygen deficient PZT 20/80 films. When comparing the experiment with the simulation results in this work, one should bear in mind that averages of any parameter for "the volume under influence around a defect" will not be the same as the "area under influence around a defect" in the 2D lattice, hence qualitatively identical results could likely be expected in the simulations at different La concentrations than that of experiment. Despite this intuitive foresight, the simulated hysteresis captures the behavior of the real samples for quite similar La concentrations. That the loss of hysteresis in the experiments with increasing La content is not a microstructural aspect but purely a lattice related phenomenon is also validated. Therefore, the results we obtain from our simulations under the assumption of donor/acceptor couples serve very well in explaining the defect-mediated loss of hysteresis and the reduction in the transition temperatures in the real samples deduced from the dielectric data.

During the simulations, we noted that a few percent La in the lattice is sufficient to alter the polarization and weaken the hysteresis, which we found to be emanating profoundly from the electrostatics associated with the donor/acceptor couples rather than the local elastic strain component of the La sites. If we turn off the electrostatic fields due to defect complexes (putting $\rho(r) = 0$ at every defect site in Eq. 30) and only consider the strain fields associated with them, no such outcome is delivered by the simulations. In fact, the hysteresis get extended along the field axis as a consequence of the localized enhancements in the Curie temperature due to strain. The inhomogeneous nature of the strains around the La sites do not have as profound an effect expected as often discussed in the light of depolarizing field effects. Whilst a partial source of the depolarization effects in ferroelectrics is the gradients in polarization, we find that the relatively gradual change of polarization in the case of local defects with a strain component do not mediate a substantial depolarizing field and local strain driven enhancement is more pronounced. Much of

the effects in the hystereses and the dielectric measurements pronounced in our work are thus conjectured to arise from the electrical fields of the donor/acceptor dipole-defect complexes near La sites. We provide the polarization amplitude maps of the 2D grid at room temperature in Figure 23 to display the highly variable distribution of the polarization due to coupling with strain and electrostatic fields of the La sites. The noticeable "noise" of the hysteresis emanate from the procedure in distributing the La sites into the 2D lattice where a lack of total randomness in the defect-dipole orientations can be observed to arise, inhibiting fully symmetrical response along both the polarization and the bias field axis. Owing to the very large system size and the granular orientations, such an effect is neither observed nor expected in experiments in contrast to the effects expected due to the finiteness of the 2D simulation grid.

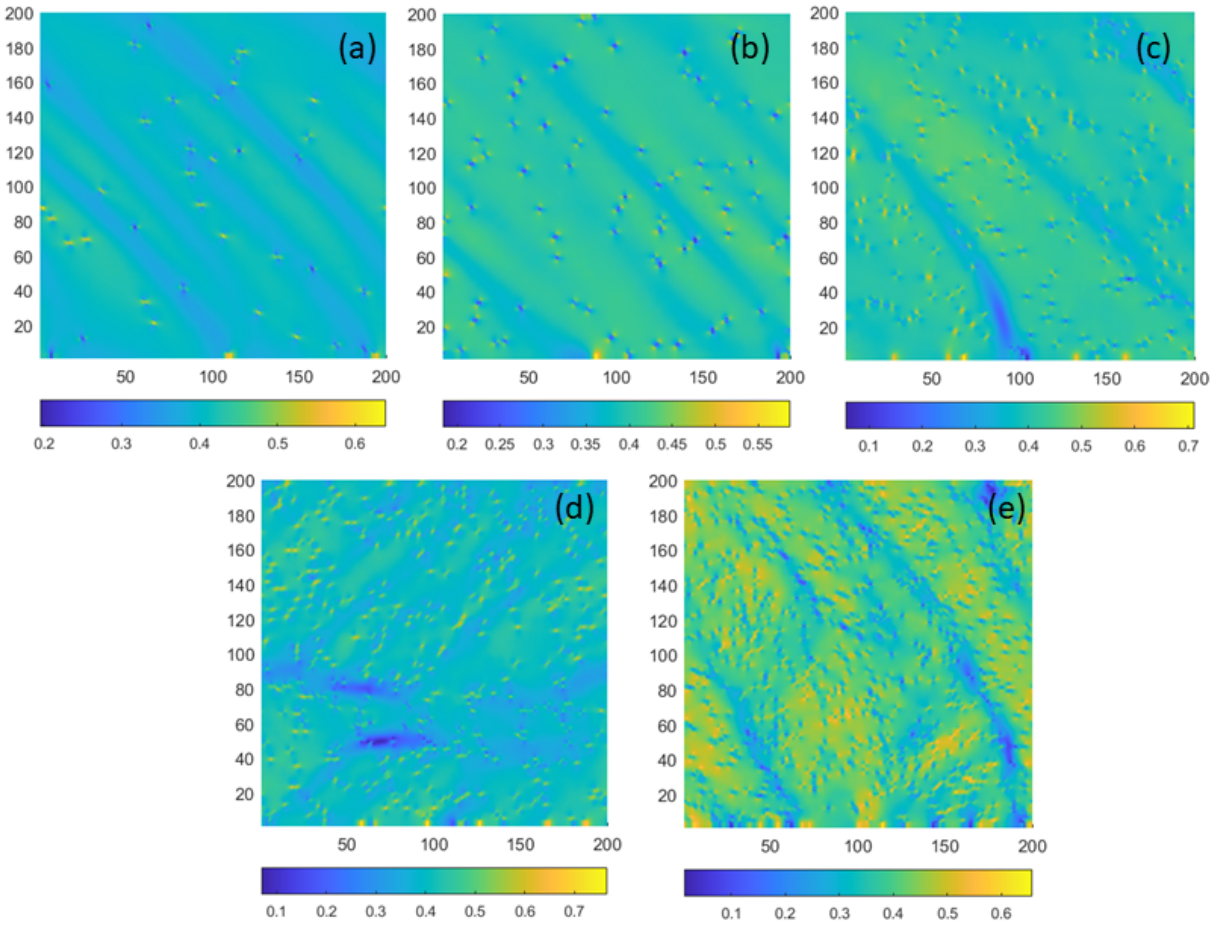

Figure 23. Simulated polarization amplitude maps ($|P|=\sqrt{P_1^2 + P_3^2}$) for (a) 0.5%, (b) 1%, (c) 2,5%, (d) 5% and (e) 10% La concentration at 0V bias and RT. Note that much of the dramatic local enhancements of |P| with increased La concentration can correspond to total energy values

exceeding that of the paraelectric phase (zero), meaning that the latter is stabilized close to RT. The La sites reveal themselves as blue/yellow spots that indicate the locally induced |P|.

Following comparison of the hysteresis behavior in the simulations with experiment, we went on to compare the trend in the reduction of the Curie temperature as a function of La content in our simulations with that of experimental ones deduced from temperature dependent dielectric measurements. The transition temperatures in experiments were estimated via checking the temperatures to which the maxima of the dielectric response curves correspond to as there is a strong smearing effect. The same strong smearing effect was also observed in the simulations where the usual criteria of labeling the temperature at which polarization becomes zero as the transition temperature was not reliable. Instead, we computed the energies as a function of temperature of the 2D grid using Eq. 24 by plugging in the solutions for polarization components, electric field, and strains for various La concentrations and denoted the temperature at which the total energy crossed zero as the transition temperature to the paraelectric state. We provide the comparison of the experimentally estimated transition temperatures with that of the simulations in Figure 24. A highly similar, negatively correlated linear trend in the transition temperatures as that in Figure 6 was also reported in the experiments in Ref. [31] but for systematically A-site doped $BiFeO_3$ along with a smearing effect.

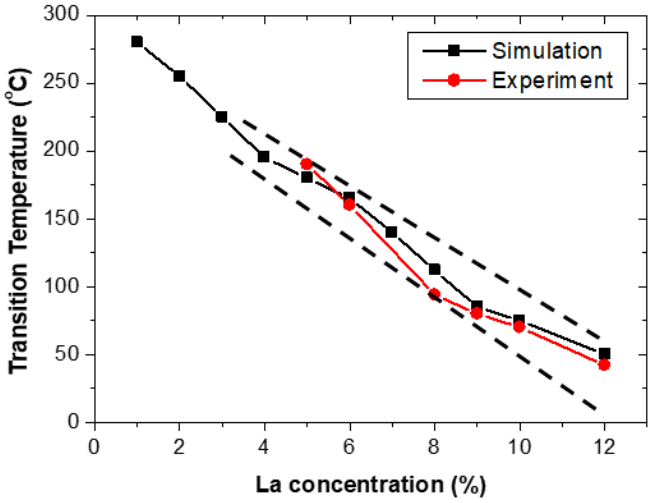

Figure 24. Transition temperatures extracted from experiments and those found via the equivalence of the paraelectric and the ferroelectric phase energies in the simulations. The dashed lines indicate the approximate limits of the values computed for the range of temperatures in the

simulations during several runs while the solid black square data points denote the averages. The transition temperature for the defect-free PZT 70/30 is ~ 330°C.

Summary and Outlook

In this project, we undertook the task of finding the dependence of the ECE induced changes in ΔT on applied field direction for stress free PMN-PT compositions in the PMN rich regime. Another part of the activity was devoted to use of doping to control the phase transition temperature of another famous composition, namely PZT 30/70 and adjust the ECE response. Applying the Landau theory of phase transitions along with incorporation of a rotated frame approach, we were able to systematically compute the field dependence of 10 different compositions 6 of which intersect the MPB in the composition vs. temperature phase diagram for a wide range of crystallographic directions. The compositions whose ground state are the r-phase exhibit lower ΔT values near their respective transition temperatures and have weak dependence on field orientation when near the MPB as expected. A higher PMN concentration favoring weak polar order in the r-phase could be an argument to hinge upon, however a few percent change in composition across the MPB near their respective transition temperatures causes more than 10% of change in maximal ΔT. The ΔT values computed for compositions in the r-phase are lower than those on the right side of the MPB, i. e., the tetragonal phase for any applied field value considering the direction along which maximal ΔT occurs. ΔT values can vary almost 20 % with applied field direction particularly in the t-phase, implying the importance of the anisotropy of the ECE that is systematically explored in our work. Change of composition, when remaining in the r-phase, can alter the ΔT vs. applied field topology wherein the direction of maximal ΔT and spontaneous polarization may differ or coincide. The latter occurs when approaching the MPB where the ΔT vs. field direction topology near the transition abruptly changes upon entering the tetragonal phase region. Results we report herein reveal a roadmap to maximize the ECE induced ΔT values for the PMN-PT system and the method can easily be adapted to other ferroelectric compositions to engineer the anisotropy in these systems to maximize the ECE.

Another emphasis of the proposal was to study the effect of dopant type defects on the ECE of ferroelectric perovskites. For this case, La doped PZT, a material that have attracted great attention for its superior properties over many other perovskite compositions, was studied. We have carried out systematic experiments in La doped PZT 70/30 composition to connect the doping process to the transition characteristics and to study the suitability of these materials for EC applications. With increasing La content, properties start to deviate from that of pure PZT 70/30 substantially

that were describable by the La sites in the lattice acting as defect-dipole complexes as revealed by thermodynamic simulations. Some of the findings we report are in contrast with the phase diagram proposed for the La-rich (>9-10%) PZT 70/30 that is also supported, albeit indirectly, by our EC analyses. Even when reaching the fields near the break down limit of PZT 70/30, we have neither observed a AFE-to-FE transition in the hysteresis nor a sudden change in the EC response that one would expect as a result of a field induced AFE-to-FE transition. The reduction and smearing of the transition temperature agree with what one would expect from an increasing concentration of lattice defects in a ferroelectric, a conjecture which we tried to prove via thermodynamic simulations. We also note that there appears to be an optimal concentration of La doping to obtain ΔT values exceeding 1K or more that is sustainable in a wide temperature range that is desirable for ECE devices. This optimal concentration falls in the phase regime where the stable state is ferroelectric with a smeared transition temperature around 85°C. Further smearing of the transition beyond 8%La concentration results in a weaker ΔT in the entire applied electric field range, likely driven by the stabilization of the paraelectric or a weak polar phase.

To maximize the ECE, one needs to have the ferroelectric material near its phase transition point. Our study suggests that the amplitude of polarization in each phase plays a greater role than tailoring of the anisotropy effects, i.e. the relation between the polar axis and the applied field direction. One important outcome of the project was the physics underlying the ECE of PMN-PT for PMN-rich compositions. Contrary to intuition, the highest ECE induced ΔT changes are computed for the tetragonal composition along directions that deviate from the axis of the spontaneous polarization. A similar study can be adapted to thin films where the possibility of applying high fields is much greater than bulk crystals. A range of suitable substrates can be used as an underlying template crystal to obtain ferroelectric thin films of a desired orientation for a systemic study of anisotropy effects. Note that the substrate will clamp the film at least along two orthogonal directions that will likely result in several dramatic changes in the transition characteristics as well as the ECE. Several questions remain as to the change of the ECE response in thin films and how domains and similar microstructures that are known to decorate films will impact the overall functionality. These are questions that can be answered in a future proposal combining experimental measurements with theory.

References

1. Khakpash, N., et al., *Misfit strain phase diagrams of epitaxial PMN-PT films.* Applied Physics Letters, 2015. **106**(8).

2. Li, Z.H., et al., *Effect of electric field orientation on ferroelectric phase transition and electrocaloric effect.* Acta Materialia, 2020. **191**: p. 13-23.

3. Chukka, R., et al., *Enhanced cooling capacities of ferroelectric materials at morphotropic phase boundaries.* Applied Physics Letters, 2011. **98**(24).

4. Perantie, J., et al., *Electrocaloric properties in relaxor ferroelectric (1-x)Pb(Mg1/3Nb2/3)O-3-xPbTiO(3) system.* Journal of Applied Physics, 2013. **114**(17).

5. Zhang, T.F., et al., *Orientation related electrocaloric effect and dielectric phase transitions of relaxor PMN-PT single crystals.* Ceramics International, 2017. **43**(18): p. 16300-16305.

6. Sebald, G., et al., *Electrocaloric and pyroelectric properties of 0.75Pb(Mg1/3Nb2/3)O-3-0.25PbTiO(3) single crystals.* Journal of Applied Physics, 2006. **100**(12).

7. Perantie, J., et al., *Electric-field-induced dielectric and temperature changes in a < 011 >-oriented Pb(Mg1/3Nb2/3)O-3-PbTiO3 single crystal.* Physical Review B, 2010. **82**(13).

8. Ponomareva, I. and S. Lisenkov, *Bridging the Macroscopic and Atomistic Descriptions of the Electrocaloric Effect.* Physical Review Letters, 2012. **108**(16).

9. Graf, M. and J. Iniguez, *A unified perturbative approach to electrocaloric effects.* Communications Materials, 2021. **2**(1).

10. Nye, J.F., *Physical Properties of Crystals*. 1985, New York: Clarendon Press Oxford

11. K. C. Cheng, H.L.W.C., C. L. Choy, Q. R. Yin, H. S. Lu, and Z. W. Yin, *Piezoelectric coefficients of PMN-0.33 PT single crystals.* Proceedings of the 2000 12th IEEE International Symposium on Applications of Ferroelectrics (IEEE Cat. No. 00CH37076), 2000. **2**: p. 533-536.

12. Aleshin, V.I. and I.P. Raevski, *Negative Poisson's ratio and piezoelectric anisotropy of tetragonal ferroelectric single crystals.* Journal of Applied Physics, 2012. **112**(11).

13. Gorev, M.V., et al., *Heat capacity study of relaxor PbMg1/3Nb2/3O3 in a wide temperature range.* Journal of Experimental and Theoretical Physics, 2003. **96**(3): p. 531-537.

14. Kobertz, D., M. Muller, and A. Molak, *Vaporization and caloric studies on lead titanate.* Calphad-Computer Coupling of Phase Diagrams and Thermochemistry, 2014. **46**: p. 62-79.

15. Wongmaneerung, R., et al., *Thermal expansion properties of PMN-PT ceramics.* Journal of Alloys and Compounds, 2008. **461**(1-2): p. 565-569.

16. Ahart, M., et al., *Pressure dependence of the monoclinic phase in (1-x)Pb(Mg1/3Nb2/3)O-3-xPbTiO(3) solid solutions.* Physical Review B, 2012. **86**(22).

17. Asbani, B., et al., *Electrocaloric response in lanthanum-modified lead zirconate titanate ceramics.* Journal of Applied Physics, 2020. **127**(22).

18. Limpichaipanit, A., et al., *Electrocaloric properties of Bi and Cu doped PLZT 9/65/35 ceramics at low electric field.* Ceramics International, 2020. **46**(4): p. 5252-5261.

19. Lu, B., et al., *Large Electrocaloric Effect in Relaxor Ferroelectric and Antiferroelectric Lanthanum Doped Lead Zirconate Titanate Ceramics.* Scientific Reports, 2017. **7**.

20. Gozuacik, N.K., E. Mensur-Alkoy, and S. Alkoy, *Effects of lanthanum doping on electrical and electromechanical properties of (Pb1-xLax)(Zr0.70Ti0.30)O-3 ceramics.* Journal of Materials Science-Materials in Electronics, 2019. **30**(15): p. 14045-14052.

21. Tong, S., et al., *Effect of dead layer and strain on the diffuse phase transition of PLZT relaxor thin films.* Acta Materialia, 2011. **59**(3): p. 1309-1316.

22. Haertling, G.H., *Plzt Electrooptic Materials and Applications - a Review.* Ferroelectrics, 1987. **75**(1-2): p. 25-55.

23. Li, J.J., et al., *Effects of Long- and Short-Range Ferroelectric Order on the Electrocaloric Effect in Relaxor Ferroelectric Ceramics.* Physical Review Applied, 2019. **11**(4).

24. Kim, D.S., et al., *Direct and indirect measurements of the electro-caloric effect in (Bi,Na)TiO3-SrTiO3 ceramics.* Journal of Applied Physics, 2019. **126**(23).

25. Poykko, S. and D.J. Chadi, *First principles study of Pb vacancies in PbTiO3.* Applied Physics Letters, 2000. **76**(4): p. 499-501.

26. Cockayne, E. and B.P. Burton, *Dipole moment of a Pb-O vacancy pair in PbTiO3 (vol 69, art no 144116, 2004).* Physical Review B, 2004. **69**(21).

27. Mestric, H., et al., *Iron-oxygen vacancy defect centers in PbTiO3: Newman superposition model analysis and density functional calculations.* Physical Review B, 2005. **71**(13).

28. Pu, Y.T., et al., *Double hysteresis loop induced by defect dipoles in ferroelectric Pb(Zr0.8Ti0.2)O-3 thin films.* Journal of Applied Physics, 2011. **109**(4).

29. Dai, X.H., et al., *Effects of lanthanum modification on rhombohedral Pb(Zr1-xTix)O-3 ceramics .2. Relaxor behavior versus enhanced antiferroelectric stability.* Journal of Materials Research, 1996. **11**(3): p. 626-638.

30. Vales-Castro, P., et al., *Origin of large negative electrocaloric effect in antiferroelectric PbZrO3.* Physical Review B, 2021. **103**(5).

31. Khodabakhsh, M., et al., *Strong smearing and disappearance of phase transitions into polar phases due to inhomogeneous lattice strains induced by A-site doping in Bi(1-x)A(x)FeO(3) (A: La, Sm, Gd).* Journal of Alloys and Compounds, 2014. **604**: p. 117-129.